

Resonant field emission from noble-metal/graphene heterostructures

Maxim Trushin*

*Institute for Functional Intelligent Materials, National University of Singapore,
4 Science Drive 2, Singapore 117544, Singapore, and
Department of Materials Science and Engineering, National University of Singapore,
9 Engineering Drive 1, Singapore 117575, Singapore*

Field emission from metals underpinned early vacuum-tube technology, and recent nanoscale engineering made field-emission devices compatible with modern silicon platforms. However, the limited tunability of electron transport in metals has restricted their applicability. Here, we show that noble metals coated with graphene exhibit clean non-monotonic $I - V$ characteristics arising from resonant tunneling through graphene's electronic states, enabled by graphene's atomic thinness and weak electronic hybridization with noble metals. Our approach combines ab-initio interface parameters with exact solutions of the Schrödinger equation for electron transmission across the interface. We analyze two experimentally relevant geometries: a vertical configuration with a flat suspended emitter and a coplanar configuration with sharp electrodes allowing for strong field enhancement and gating. These results establish a practical route to tunable electron transport in metal heterostructures, positioning them as competitive components for air-channel field-emission nanoelectronics.

Keywords: air-channel field emission, graphene, metallic heterostructures

Field emission has been studied for more than a century [1], with Fowler-Nordheim (FN) theory describing electron tunneling from metallic conduction-band states under strong electric fields [2]. When vacuum channels are downscaled to tens of nanometers [3–7], and even below 10 nm [8], measured currents generally follow FN scaling, with platinum contacts as a notable exception [5]. Resonant tunneling, initially introduced by placing a single atom at an emitter tip, can substantially enhance field emission at nanoscale [9]. It can also be engineered via emitter nanostructuring and has been demonstrated using thin Si/SiO₂ [10] and carbon [11] layers, as well as silicon nanostructures [12, 13]. Resonant FN tunneling can also be induced by atomically thin dielectrics on the emitter surface [14, 15], and has been analyzed by solving the one-dimensional Schrödinger equation numerically [16] or analytically [14, 17]. More recently, transfer-matrix methods have been used [18].

Field-emission devices have experienced a revival with the advent of air-channel architectures that conduct current across ~ 10 nm gaps where electron-molecule collisions are negligible [5]. Compared with traditional vacuum electronics, such extreme downscaling reduces operating voltages to CMOS-compatible levels [19, 20] and enables integration with semiconductor platforms [21–24], opening opportunities for high-speed, robust operation [25, 26]. Nanoscale electrode geometries further concentrate local fields, yielding large enhancement factors [8, 27]. Within this context, resonant field emission offers a pathway to engineered, non-monotonic $I - V$ characteristics for air-channel nanoelectronics.

In this Letter, we propose using two-dimensional (2D) conductors to harness and tune resonant tunneling for field emission. In materials such as graphene [28] and emerging 2D metals [29], out-of-plane electron motion

is in the ultra-quantum limit and effectively confined to a single 2D subband. When such a conductor is physisorbed on a bulk metal, the angstrom-scale interfacial gap can support a clean, single resonance in the tunneling probability, yielding pronounced, tunable enhancements in emission near a characteristic field. We develop this concept using noble-metal/graphene heterostructures, which form well-defined angstrom-scale interfaces [30–32], and we ground the analysis in ab initio interface parameters and exact solutions of the Schrödinger equation for transmission across the junction.

Figure 1 summarizes the central result by contrasting resonant emission with classical FN tunneling and illustrating a vertical noble-metal/graphene nanobridge emitter above a doped-Si collector. We examine Au, Pt, and Ag contacts, focusing on gold because ARPES measurements for graphene on Au [31] align closely with the ab initio interface parameters used in our simulations. We then analyze finite-size effects, including the transition to direct tunneling, surface roughness, and electrode curvature, and finally demonstrate resonant field emission in a coplanar geometry with sharp electrodes that enable strong field enhancement.

Strong out-of-plane confinement in a 2D conductor quenches the electron kinetic energy along the out-of-plane direction, creating a theoretical challenge for describing out-of-plane emission [33–36]; see also recent reviews [37, 38]. Consequently, the central ingredient in modeling electron emission through a 2D material is the choice of the out-of-plane confining potential. A minimal and effective way to model this confinement is a delta-function potential, $-u_0\delta(z)$, which captures the ultra-quantum limit with a single out-of-plane subband, see Fig. 1(a). In this framework, the potential

Metal	W_m (eV)	W (eV)	ΔE_F (eV)	$\Delta V/d$ (eV/Å)
Ag	4.92	4.24	-0.32	0.20
Au	5.54	4.74	+0.19	0.24
Pt	6.13	4.87	+0.33	0.38

TABLE I. Work functions of bulk metals (W_m) and graphene (W) adsorbed on their surfaces, computed via DFT [43], with electron transfer captured by the Fermi energy shift in graphene (ΔE_F). The interfacial barrier is characterized by $\Delta V = W_m - W$ and an interlayer spacing d of about 3.3Å, computed within the same ab-initio approach [42, 43] used to match the band parameters measured by ARPES [31].

strength $u_0 > 0$ sets both the work function and the decay length: $W_0 = mu_0^2/(2\hbar^2)$ and $l_0 = \hbar^2/(mu_0)$, where \hbar is the reduced Planck constant, m is the free electron mass governing out-of-plane motion. A full derivation of graphene's electronic states under delta-function confinement is provided in Supporting Information S1.

The functionality of the proposed device relies on graphene physisorbing, rather than chemisorbing, onto a noble-metal surface. Chemisorption alters graphene's band structure and reduces the graphene-metal separation d to 2–2.5 Å, whereas physisorption preserves graphene's electronic structure at larger separations ($d > 3$ Å) [39]. Note that d differs from the AFM-measured graphene-substrate offset, which includes the full graphene thickness and interfacial contaminants [40]. High-resolution ARPES confirms physisorption on iridium [30] and gold [31], where graphene retains its gapless Dirac dispersion, in contrast to nickel [41] and copper [31], which induce stronger hybridization. Even in the physisorbed regime, however, proximity-induced charge transfer can dope graphene and shift its Fermi level by ΔE_F , changing the work function to $W = W_0 + \Delta E_F$ [42]. Crucially, electron transfer does not fully equilibrate the work functions in graphene (W) and metal (W_m): an interface dipole layer forms and maintains a finite barrier $\Delta V = W_m - W$ [43], which separates graphene's 2D states from the bulk metal states. We model this interfacial barrier as trapezoidal with a constant potential gradient $\Delta V/d$, see Fig. 1(b), and its parameters are obtained by fitting density-functional theory (DFT) data [42] to a phenomenological model [43]. A summary of W_m , W , ΔE_F , and ΔV is provided in Table I.

To describe field emission, we introduce the conduction-band depth in the bulk, $V_0 - E_F$, typically about 5 eV in noble metals, and the external field \mathcal{E}_{ext} , see Fig. 1(c). Given the high electron concentration in noble metals, we assume E_F and ΔV are unaffected by emission. The emission current is computed from the exact solution of the Schrödinger equation for out-of-plane electron motion in the potential profile shown in Fig.1(c), with the Hamiltonian $\hat{H} = \hbar^2 \hat{k}_z^2/(2m) + U(z)$, where

$k_z = -i\partial/\partial z$, and $U(z)$ reads

$$U(z) = -u_0\delta(z) + \begin{cases} e\mathcal{E}_{\text{ext}}z, & z < 0, \\ \Delta Vz/d, & 0 < z < d, \\ -V_0, & z \geq d; \end{cases} \quad (1)$$

where e is the elementary charge. The solution to the Schrödinger equation can be written as

$$\psi(z) = \begin{cases} A_1 [\text{Ai}(\zeta_1) + i\text{Bi}(\zeta_1)], & z < 0, \\ A_2 \text{Ai}(\zeta_2) + B_2 \text{Bi}(\zeta_2), & 0 < z < d, \\ A_3 e^{-ikz} + B_3 e^{ikz}, & z > d; \end{cases} \quad (2)$$

$$\zeta_1 = -\frac{E_k}{e\mathcal{E}_{\text{ext}}z_1} + \frac{z}{z_1}, \quad z_1 = \left(\frac{\hbar^2}{2m\mathcal{E}_{\text{ext}}}\right)^{\frac{1}{3}}, \quad (3)$$

$$\zeta_2 = -\frac{E_k d}{\Delta V z_2} + \frac{z}{z_2}, \quad z_2 = \left(\frac{\hbar^2 d}{2m\Delta V}\right)^{\frac{1}{3}}, \quad (4)$$

$$k = \sqrt{\frac{2m}{\hbar^2}(V_0 + E_k)}, \quad (5)$$

where $\text{Ai}(\zeta_{1,2})$, $\text{Bi}(\zeta_{1,2})$ are Airy functions. The coefficients are found by matching the wave function and its derivative at $z = 0$ and $z = d$. This results in four equations given by

$$A_1 [\text{Ai}(\zeta_{10}) + i\text{Bi}(\zeta_{10})] = A_2 \text{Ai}(\zeta_{20}) + B_2 \text{Bi}(\zeta_{20}), \quad (6)$$

$$\begin{aligned} & \frac{A_1}{z_1} [\text{Ai}'(\zeta_{10}) + i\text{Bi}'(\zeta_{10})] - \frac{1}{z_2} [A_2 \text{Ai}'(\zeta_{20}) + B_2 \text{Bi}'(\zeta_{20})] \\ &= \frac{2}{l_0} [A_2 \text{Ai}(\zeta_{20}) + B_2 \text{Bi}(\zeta_{20})], \end{aligned} \quad (7)$$

$$A_2 \text{Ai}(\zeta_{2d}) + B_2 \text{Bi}(\zeta_{2d}) = A_3 e^{-ikd} + B_3 e^{ikd}, \quad (8)$$

$$\begin{aligned} & \frac{1}{z_2} [A_2 \text{Ai}'(\zeta_{2d}) + B_2 \text{Bi}'(\zeta_{2d})] \\ &= -ikA_3 e^{-ikd} + ikB_3 e^{ikd}, \end{aligned} \quad (9)$$

where $\text{Ai}'(\zeta_{1,2})$, $\text{Bi}'(\zeta_{1,2})$ are derivatives of the Airy functions with $\zeta_{10} = \zeta_1(z = 0)$, $\zeta_{20} = \zeta_2(z = 0)$, $\zeta_{2d} = \zeta_2(z = d)$. Solving Eqs. (6–9) yields $A_{1,2,3}$ and B_2 . The incident, reflected, and transmitted probability current densities are, respectively, given by

$$j_i = \frac{\hbar k}{m}|B_3|^2, \quad j_r = \frac{\hbar k}{m}|A_3|^2, \quad j_t = \frac{\hbar}{\pi m z_0}|A_1|^2, \quad (10)$$

where we have used the identity

$$\text{Ai}(\zeta)\text{Bi}'(\zeta) - \text{Ai}'(\zeta)\text{Bi}(\zeta) = 1/\pi. \quad (11)$$

By convention, we take $k < 0$ for the incident current propagating toward $z \rightarrow -\infty$, and we set $B_3 = 1$ for normalization. The transmission and reflection probabilities then read

$$T = \frac{j_t}{j_i}, \quad R = \frac{j_r}{j_i}, \quad (12)$$

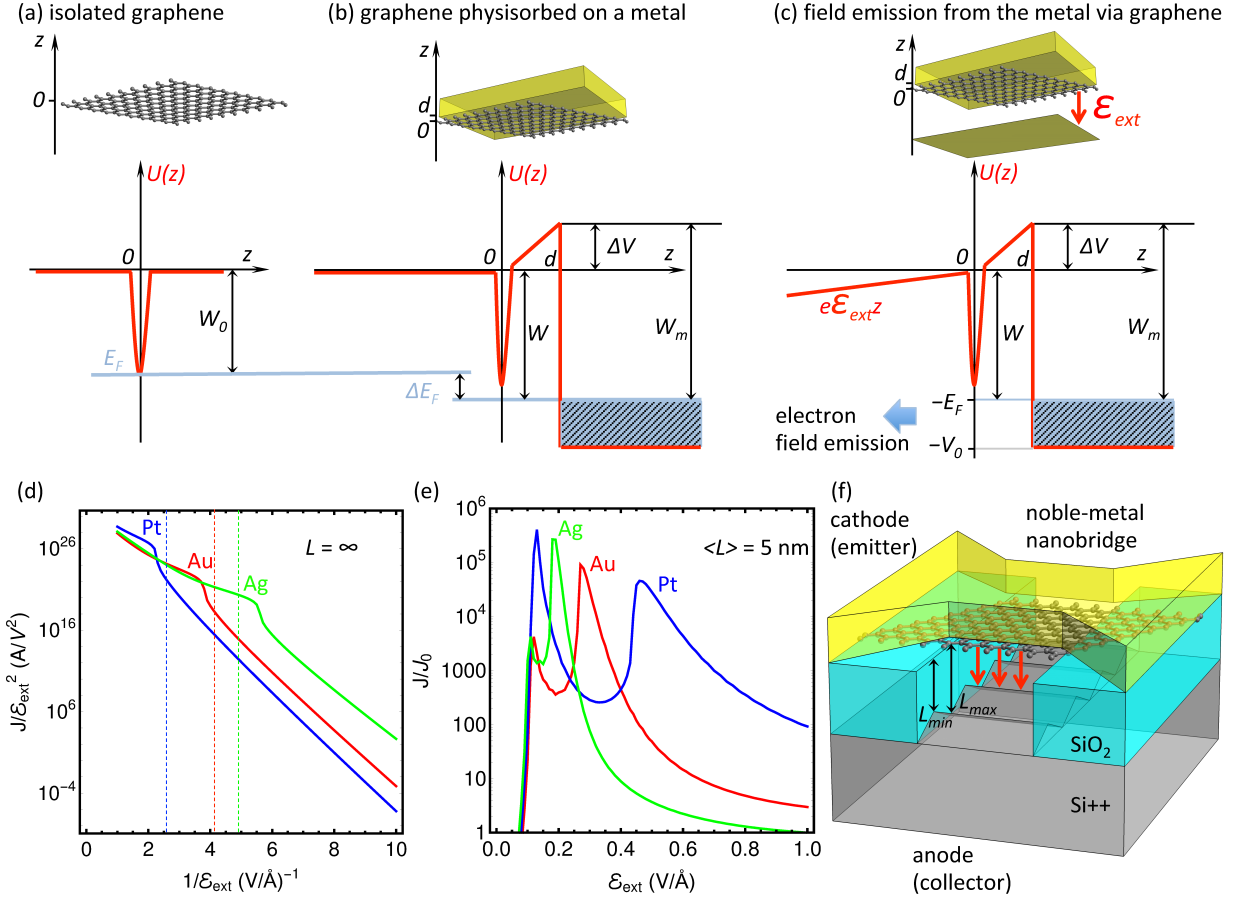


FIG. 1. Resonant field-emission by metal-graphene interface. (a) Out-of-plane potential profile of isolated graphene exhibits extremely narrow electron confinement, with the work function $W_0 = 4.55$ eV. (b) Upon physisorption on a metal, the work function difference leads to a redistribution of surface charge, shifting the Fermi level by ΔE_F in graphene and creating an interfacial barrier of height ΔV and thickness d . (c) Field electron emission from a metal covered by graphene is governed by tunneling through a composite potential barrier consisting of triangular and trapezoid sections, which supports a resonant state. (d) Fowler-Nordheim representation of the field-emission current density J clearly demonstrates deviation from the conventional linear relation between $\ln(J/\mathcal{E}_{\text{ext}}^2)$ and $1/\mathcal{E}_{\text{ext}}$ when $e\mathcal{E}_{\text{ext}} \sim \Delta V/d$ (shown by dashed lines) and the resonant level enters the energy window between $-E_F$ and $-V_0$, see Fig. 2. The exact position of the emission maximum also depends on charge doping, which can be either n - or p -type (negative or positive ΔE_F ; see Table I), depending on a metal employed (Ag, Au, and Pt). The finite-size channel effects are neglected here (no direct tunneling, see Fig. 3). (e) Field emission current density computed for the device shown in (f) and normalized to J_0 computed for the same geometry without graphene. The curves are averaged over 100 channels of randomized lengths between $L_{\text{min}} = 4.5$ nm and $L_{\text{max}} = 5.5$ nm to take into account the collector surface roughness. The model neglects the field enhancement factors (e.g. the image-charge effects), which are addressed in Fig. 4. (f) Possible realization of the resonance field-emission on a heavily doped Si/SiO₂ wafer with a bow-tie gold bridge and SiO₂ etched away underneath, see Ref. [44]. Doped Si is usually used as a gate contact but if SiO₂ is removed completely under the nanobridge, it plays an electron collector role.

which satisfy $T + R = 1$.

The field emission current can be written as an integral over $j_t(k)$ and is given by

$$J = 2e \int \frac{dk}{2\pi} \int \frac{d^2 k_{\parallel}}{(2\pi)^2} j_t(k), \quad (13)$$

where we integrate over in-plane (k_{\parallel}) and out-of-plane ($k > 0$) wave vectors. The Fermi level sets the integral limits as $k_{\parallel} \leq \sqrt{\frac{2m}{\hbar^2}(-E_k - E_F)}$ and $k \leq \sqrt{\frac{2m}{\hbar^2}(V_0 - E_F)}$. Here, $E_k = -V_0 + \hbar^2 k^2/(2m)$ and

$E_F = W_0 + \Delta E_F$, see Fig. 1(a-c) and Table I. The electron effective mass (m) and conduction band depth $V_0 - E_F \sim 5$ eV are taken to be the same for all the metals considered, as their particular values have negligible effects on the resonant emission. Taking the integral over k_{\parallel} and changing the variable dk to dE_k (see Supporting Information S2) we arrive at the final expression for J

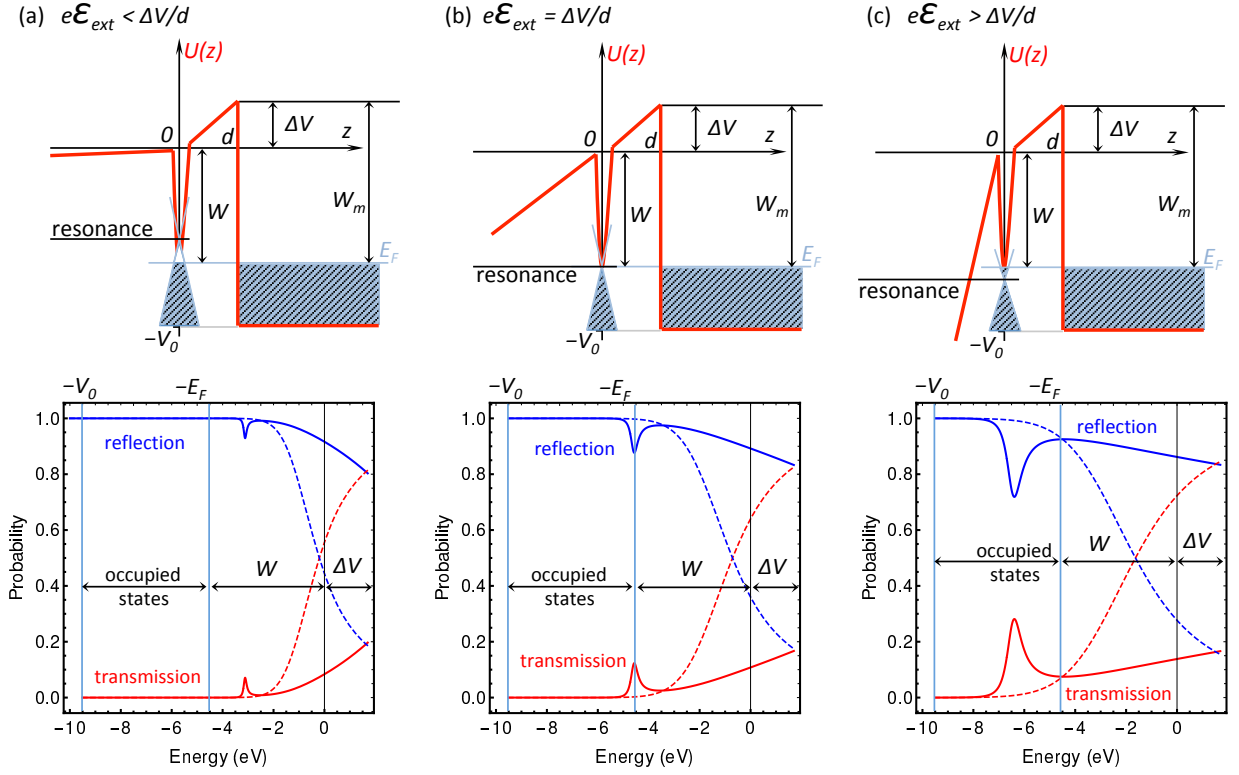


FIG. 2. Resonant features in transmission (red) and reflection (blue) probabilities with (solid) and without (dashed) graphene. Parameters are chosen such to make the resonance clearly visible, $W_m = 6.2$ eV, $W = 4.5$ eV, $\Delta E_F = 0$, $V_0 = 9.5$ eV, $d = 0.17$ nm, and they do not correspond to a specific metal. (a) For $e\mathcal{E}_{\text{ext}} < \Delta V/d$, the resonance lies above the Fermi level; emission from occupied states occurs via resonance broadening. (b) For $e\mathcal{E}_{\text{ext}} = \Delta V/d$, the resonance matches the Fermi level, producing a dramatic increase in emission. (c) For $e\mathcal{E}_{\text{ext}} > \Delta V/d$, the resonance falls within the occupied energy window between the metal conduction-band bottom and the Fermi level. At such high fields, however, non-resonant emission without graphene also becomes efficient, reducing J/J_0 . With further increase of \mathcal{E}_{ext} the resonance exit the occupied energy window and the emission current drops to the non-resonant values.

given by

$$J = \frac{e}{8\pi^2} \left(\frac{2m}{\hbar^2} \right)^{\frac{3}{2}} \int_{-V_0}^{-E_F} dE_k \frac{-E_F - E_k}{\sqrt{V_0 + E_k}} \times j_t \left(\sqrt{\frac{2m}{\hbar^2} (V_0 + E_k)} \right). \quad (14)$$

Figure 1(d) shows the emission current density J for three noble-metal/graphene heterostructures (Ag, Au, and Pt), plotted on a log-scale as $J/\mathcal{E}_{\text{ext}}^2$ versus $1/\mathcal{E}_{\text{ext}}$. While a linear dependence is expected in the FN regime (see Supporting Information S2), the response here is nonmonotonic, exhibiting a single resonance near $e\mathcal{E}_{\text{ext}} \sim \Delta V/d$.

Figure 1(e) presents the resonant field emission for the same noble-metal/graphene heterostructures as in Fig. 1(d), now evaluated for the specific device shown in Fig. 1(f). The current density J is normalized to J_0 , com-

puted for the corresponding metal under the same conditions but without graphene. The simulations incorporate finite-size effects (an average emitter-collector distance separation $\langle L \rangle = 5$ nm), as well as collector surface unevenness inevitable upon etching SiO_2 away [44] (see Supporting Information S3 for details). A clear, orders-of-magnitude enhancement in current is observed near the resonant field $e\mathcal{E}_{\text{ext}} \sim \Delta V/d$.

Figure 2(a-c) illustrates resonant field emission through graphene under the simplifying assumption that graphene's work function W does not change upon contact with a metal and remains equal to that of pristine (intrinsic) isolated graphene. This is the assumption made in only Fig. 2 and Fig. 3 to demonstrate the basics of the model. The interfacial barrier $\Delta V = W_m - W > 0$ is thus taken to be constant. The band-crossing (charge-neutrality) point can be shifted upward by ΔV or downward by an external field \mathcal{E}_{ext} , as modeled in Supporting Information S1. In the limit $e\mathcal{E}_{\text{ext}} \ll \Delta V/d$, the band-

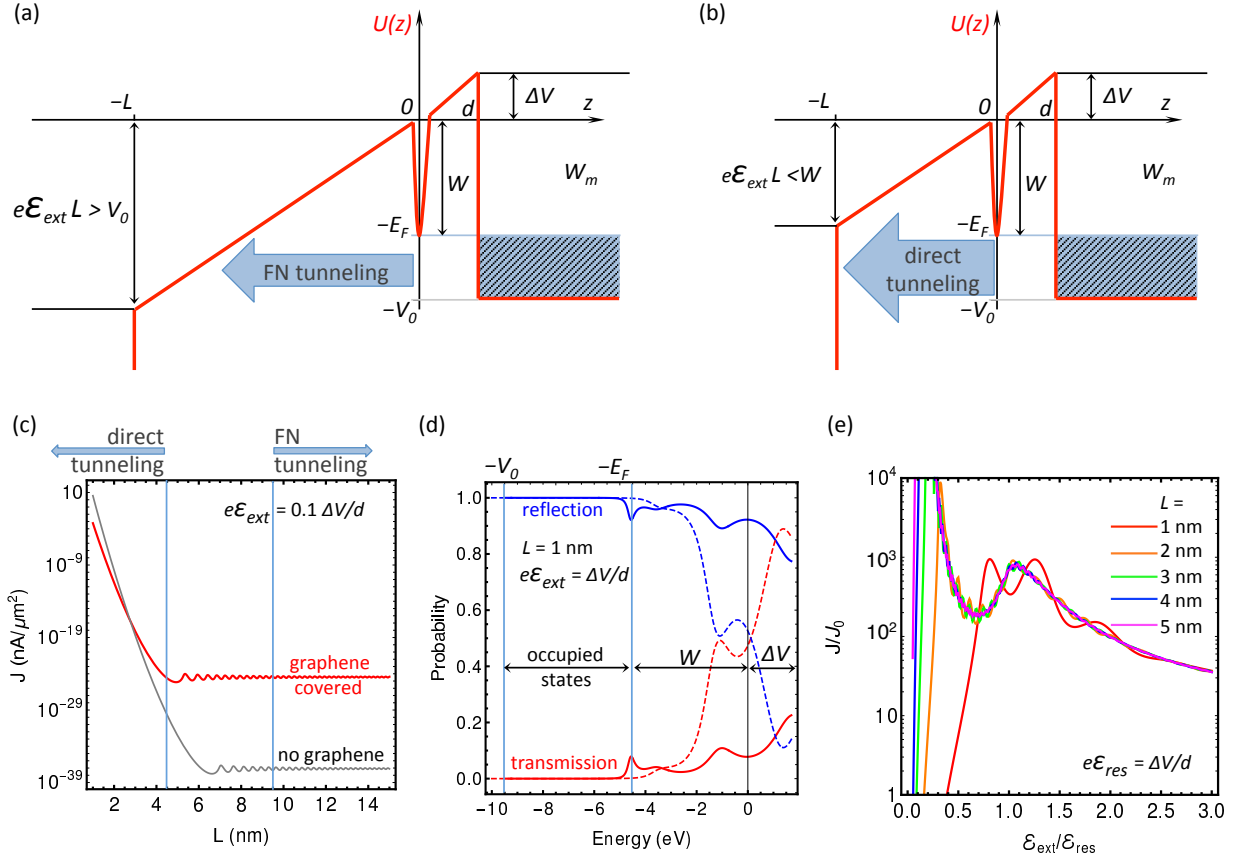


FIG. 3. Effects of finite channel length L . Parameters are the same as in Fig. 2 and do not correspond to a specific metal. (a,b) Potential profiles for FN ($e\mathcal{E}_{\text{ext}}L > V_0$) and direct tunneling ($e\mathcal{E}_{\text{ext}}L < W$) regimes, respectively. The intermediate field range $W \leq e\mathcal{E}_{\text{ext}}L \leq V_0$ corresponds to a transitional regime in which part of the occupied states tunnel via FN and the remainder via direct tunneling. (c) Distinction between FN and direct tunneling. In direct tunneling, the emission current decreases exponentially with increasing L , whereas in the FN regime it is essentially independent of L . Moreover, graphene reduces the direct-tunneling current compared with bare metal, while enhancing emission in the FN regime. (d) Transmission (red) and reflection (blue) probabilities with (solid) and without (dashed) graphene for a finite channel length of 1 nm, showing additional resonance-like features due to Fabry-Perot interference, cf. Fig. 2(b). (e) Field-emission current ratio J/J_0 versus $\mathcal{E}_{\text{ext}}/\mathcal{E}_{\text{res}}$, computed for different L , where $e\mathcal{E}_{\text{res}} = \Delta V/d$ and J_0 is the current for the same channel without graphene. In the direct-tunneling regime, the resonance maximum is distorted by backscattering between the electrodes.

crossing point is pushed to its highest energy set by ΔV and d ; in the opposite limit $e\mathcal{E}_{\text{ext}} \gg \Delta V/d$, it is lowered and governed by \mathcal{E}_{ext} . When the external and built-in fields balance ($e\mathcal{E}_{\text{ext}} = \Delta V/d$), the situation reduces to intrinsic graphene, with the Fermi level intersecting the band-crossing point.

The lower panels of Fig. 2(a-c) show that the resonance peak in the transmission probability can be tuned by \mathcal{E}_{ext} in the same way as the band shifts: the peak moves to lower energy with increasing \mathcal{E}_{ext} , and the shift becomes noticeable when $e\mathcal{E}_{\text{ext}}$ is of the order of $\Delta V/d$. The parameter values given in the figure caption are chosen to clearly demonstrate the resonance peak; unlike Fig. 1, they do not correspond to a specific metal. In realistic models, ΔV is typically much smaller and d somewhat

larger, which results in a much narrow resonance that is harder to resolve in the plot. Increasing \mathcal{E}_{ext} not only shifts the resonance but also broadens it, because the quasibound state becomes short-lived, leading to smeared resonance features. If graphene is removed, then both transmission and reflection probabilities become featureless, see Supporting Information S2.

The transmission probability itself does not depend on the Fermi level, however, the Fermi level determines whether a given transmission mode contributes to field emission. In the simplified model shown in Fig. 2(a-c), the resonant level aligns with the Fermi level at $e\mathcal{E}_{\text{ext}} = \Delta V/d$ and begins to contribute to electron emission strongly that manifests as an exponential burst in the emission current density compared with the case

without graphene. In real metals, graphene-metal heterostructures are characterized not only by the interfacial barrier height ΔV but also the Fermi-level shift ΔE_F (see Table I). For silver contacts, $\Delta E_F < 0$, which lowers graphene's work function. As a consequence, the resonant mode drops below the Fermi level and starts contributing to emission after $1/e\mathcal{E}_{\text{ext}}$ reaches $d/\Delta V$, see the green curve in Fig. 1(d). In contrast, gold and platinum induce p -type doping in graphene ($\Delta E_F > 0$), increasing its work function, so the resonant mode requires $1/e\mathcal{E}_{\text{ext}} < d/\Delta V$ to contribute, see the red and blue curves in Fig. 1(d). Because ΔV is nearly twice as large for platinum as for gold or silver, the corresponding critical $1/\mathcal{E}_{\text{ext}}$ is also about twice as low.

To elucidate the role of channel length, we contrast FN and direct-tunneling regimes, see Fig. 3(a,b). The solution follows the classical FN procedure, augmented by an additional boundary condition at $z = -L$ (see Supporting Information S3). In the FN regime, the barrier shape is set by the external field, so electrode geometry has little effect on the tunneling probability. This is a well-known property that makes FN tunneling robust, albeit requiring strong fields. The emission starts transitioning from FN to direct tunneling when the gap length L becomes smaller than $W/(e\mathcal{E}_{\text{ext}})$. The triangular barrier is then truncated to a trapezoidal one, with the truncation set by L . While the FN current is essentially independent of L , in the direct-tunneling regime the current decreases exponentially with increasing L , see Fig. 3(c). In addition, backscattering between the contacts produces Fabry-Perot-like interference in the transmission, see Fig. 3(d), leading to oscillatory features in the emission current that can partially mask the primary resonance at shorter L , see Fig. 3(e). Finally, the ratio J/J_0 drops in the direct-tunneling regime, which dominates at weaker fields.

With the length-dependent model in hand, we can simulate realistic nanometer-scale devices. Arbitrary electrode pairs can be treated by partitioning each surface into small planar facets (Supporting Information S3), yielding a set of emission channels, each defined by a local gap length L_n and by the local field component normal to the surface. Surface roughness, such as that indicated for the anode in Fig. 1(e), can be incorporated by randomizing L_n within $[L_{\text{min}}, L_{\text{max}}]$. Averaging over on the order of a hundred channels produces a smooth $I-V$ curve that retains the prominent resonance feature.

Within the FN regime, however, it is useful to distinguish smooth from sharp roughness. For smooth roughness, where graphene conforms to the metal and the graphene-metal separation d remains approximately constant, the resonance is preserved. For sharp roughness, graphene may sag locally or partially delaminate, producing spatial variations in d . In this case, each channel resonates at a slightly different field, yielding a broadened yet still identifiable resonance peak, provided d fluctuates

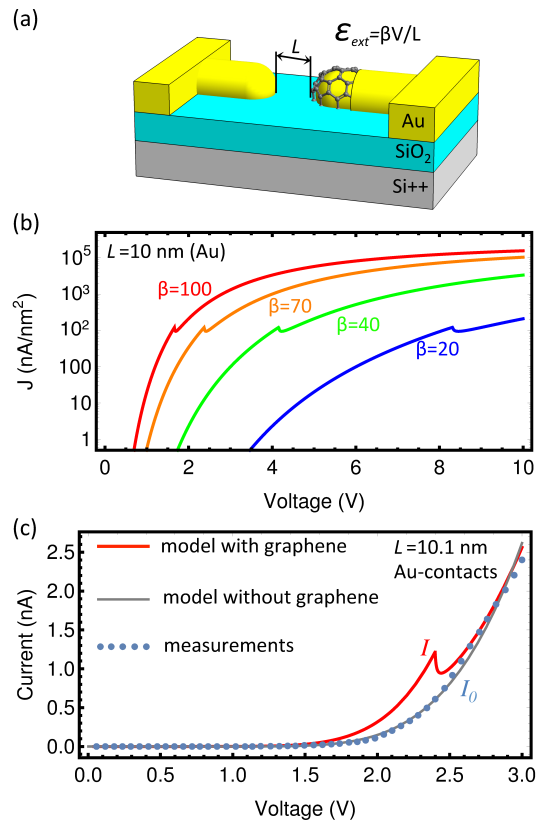


FIG. 4. Mapping the model to a coplanar device geometry with pointy contacts. (a) Possible schematics of a resonant field-emission device. The graphene layer is not to scale. The doped Si/SiO₂ substrate can be used for electrostatic gating [5]. (b) Current density versus applied voltage for a gold/graphene emitter, computed for different β values; other parameters are taken from Table I. (c) Current-voltage characteristics for a specific device with $L = 10.1$ nm and $\beta = 70$. Gray curve is obtained by fitting the field-emission model to experimental data (blue dots) for bare gold electrodes [8]. Red curve is computed using the same geometric parameters but with a graphene-coated emitter. The model predicts a resonance near $V \sim 2.3$ V.

within $1-2 \text{ \AA}$, see Supporting Information S3.

Figure 4 examines the field-enhancement factor β [37, 45], which captures image-charge and geometric effects, and is specific to each device. Because β is especially pronounced for pointy contacts [27], we adopt a coplanar geometry with sharp electrodes, see Fig. 4(a), similar to recent experimental setups [5, 8]. The applied voltage V relates to the external field as $\mathcal{E}_{\text{ext}} = \beta V/L$, where L is the electrode separation. Figure 4(b) shows resonant field-emission current density versus V for typical β and L values, demonstrating that the emission can be tuned to resonance at voltages of a few volts.

To address a finite curvature of the emitter's tip, each surface is partitioned into infinitesimal planar facets, as in the roughness modeling of Fig. 1(e,f). With finite curvature, the local field direction varies across the sur-

face; this is included by projecting \mathcal{E}_{ext} onto each facet's normal. Using this approach, we simulate electrodes of radius 10 nm for several characteristic separations (Supporting Information S3). The results show that emission is dominated by the central channel at the apex, where the local field aligns with the shortest tunneling path, consistent with established field-emission theory.

We determine β by fitting recent experimental data on field-emission from gold nanorods [8], writing $I_0 = AJ_0$, where A is an effective emission area adjusted to match the measurements. Keeping the same geometry, we then predict the $I - V$ characteristics for a graphene-coated emitter. Figure 4(c) shows that I_0 reproduces the field-emission data for bare gold nanorodes with $L = 10.1$ nm. For this relatively large gap, low-voltage direct tunneling is much weaker than high-voltage FN emission, so the latter dominates in $I_0(V)$. Using the same β and A as for I_0 , the computed $I = AJ$ (red curve) reveals substantial enhancement, and, critically, a resonant peak near $V \sim 2.3$ V. A region of negative differential conductance appears between 2.3 and 2.5 V. At higher voltages, $I_0(V)$ and $I(V)$ converge, as non-resonant emission becomes comparable to the resonant channel.

To conclude, two device geometries emerge from this work, each with distinct trade-offs. The suspended nanobridge leverages established fabrication [44] and fully exploits the spatially uniform resonant emission provided by a flat emitter. Its main limitation is electrostatic control: with the doped-Si collector serving as the anode, conventional back-gating is not available. This could be mitigated by side-gate electrodes, or a split collector [46, 47]. In contrast, the coplanar pointed electrodes readily support gating, as demonstrated experimentally [5], and benefit from large field-enhancement factors. However, conformal graphene coating is more challenging, though feasible for related architectures (e.g., nanoparticle arrays [48]).

Beyond monolayer graphene, the model naturally generalizes to multilayers by replacing a single δ -function with a stack of δ -potentials. A double-layer example (Supporting Information S1) reproduces bilayer-graphene band splitting [49], as well as field- or proximity-induced symmetry breaking. Qualitatively, each additional layer introduces an extra resonance and inter-resonance interference akin to Fig. 3(d). This provides added tunability but increases the risk of spectral overlap and inhomogeneous broadening. Practically, we expect clean, resolvable features for one to two layers, provided d fluctuations remain within 1–2 Å.

Alternative 2D coatings merit consideration. In contrast to graphene, semiconducting 2D transition metal dichalcogenides (2D TMDC), such as MoS_2 or WSe_2 , exhibit substantial hybridization on noble metals [50], which invalidates a simple trapezoidal interfacial barrier and complicates out-of-plane confinement. That said, hybridization is interface-dependent: passivation layers

(e.g., by an hBN spacer) or specific metals can restore weak coupling and a clean barrier. However, 2D TMDC thickness (up to three atomic layers) also challenge the single- δ potential approximation. More complex stacks, such as 2D metals encapsulated by pair of 2D TMDCs layers [29, 51, 52], or Janus 2D TMDCs [53–55] offer additional tuning knobs (built-in dipoles, internal polarization) but introduce intricate interfacial electronic structure that may obscure a single sharp resonance without careful engineering.

In summary, noble-metal/graphene heterostructures offer a practical route to resonant field emission with angstrom-scale interfaces, minimal hybridization, and a single out-of-plane subband — all conducive to a strong, tunable resonance at technologically reasonable voltages. The resulting non-monotonic $I - V$ characteristics with a pronounced negative differential conductance create opportunities for compact oscillators and other electronic components that remain robust at elevated temperatures. Near-term priorities include: (i) scalable graphene coating of pointed electrodes, (ii) precise control and metrology of d , and (iii) validation of resonance position and linewidth versus geometry and environment. These steps will clarify the performance envelope and integration pathways alongside air-channel nanoelectronics.

I thank Davit Ghazaryan for discussions. This research is supported by the Singapore Ministry of Education Research Centre of Excellence award to the Institute for Functional Intelligent Materials (I-FIM, Project No. EDUNC-33-18-279-V12).

* mxt@nus.edu.sg

- [1] Joseph John Thomson, “XL. cathode rays,” *Philosophical Magazine Series 5* **44**, 293–316 (1897).
- [2] Ralph Howard Fowler and Lothar Nordheim, “Electron emission in intense electric fields,” *Proceedings of the Royal Society of London. Series A* **119**, 173–181 (1928).
- [3] Jin-Woo Han, Dong-Il Moon, and M Meyyappan, “Nanoscale vacuum channel transistor,” *Nano Letters* **17**, 2146–2151 (2017).
- [4] Jin-Woo Han, Myeong-Lok Seol, Dong-Il Moon, Gary Hunter, and M Meyyappan, “Nanoscale vacuum channel transistors fabricated on silicon carbide wafers,” *Nature Electronics* **2**, 405–411 (2019).
- [5] Shruti Nirantar, Taimur Ahmed, Guanghui Ren, Philipp Gutruf, Chenglong Xu, Madhu Bhaskaran, Sumeet Walia, and Sharath Sriram, “Metal–air transistors: Semiconductor-free field-emission air-channel nanoelectronics,” *Nano Letters* **18**, 7478–7484 (2018).
- [6] Marco Turchetti, Yujia Yang, Mina Bionta, Alberto Nardi, Luca Daniel, Karl K Berggren, and Phillip D Keathley, “Electron emission regimes of planar nano vacuum emitters,” *IEEE Transactions on Electron Devices* **69**, 3953–3959 (2022).
- [7] Su Jin Heo, Jeong Hee Shin, Byoung Ok Jun, and Jae Eun Jang, “Vacuum tunneling transistor with nano

- vacuum chamber for harsh environments,” *ACS Nano* **17**, 19696–19708 (2023).
- [8] Kexin Wang, Zhaoxuan Zhang, Suhui Zhang, Huiyan Jiang, and Wei Sun, “Enhancing field emission in air via ultrascaled nanorod electrodes,” *Nano Letters* **24**, 10047–10054 (2024).
 - [9] Vu Thien Binh, S T Purcell, N Garcia, and J Doglioni, “Field-emission electron spectroscopy of single-atom tips,” *Phys. Rev. Lett.* **69**, 2527–2530 (1992).
 - [10] V G Litovchenko, A A Evtukh, Yu M Litvin, N M Goncharuk, and V E Chayka, “Observation of the resonance tunneling in field emission structures,” *Journal of Vacuum Science & Technology B: Microelectronics and Nanometer Structures Processing, Measurement, and Phenomena* **17**, 655–658 (1999).
 - [11] V Litovchenko, A Evtukh, Yu Kryuchenko, N Goncharuk, O Yilmazoglu, K Mutamba, H L Hartnagel, and D Pavlidis, “Quantum-size resonance tunneling in the field emission phenomenon,” *Journal of Applied Physics* **96**, 867–877 (2004).
 - [12] S Johnson, U Züllicke, and A Markwitz, “Universal characteristics of resonant-tunneling field emission from nanostructured surfaces,” *Journal of Applied Physics* **101**, 123712 (2007).
 - [13] Mykola Semenenko, Serhii Antonin, Roman Redko, Yuriy Romanuyk, Alexandra V Hladkovska, Viacheslav Solntsev, and Anatoliy Evtukh, “Resonant tunneling field emission of Si sponge-like structures,” *Journal of Applied Physics* **128**, 114302 (2020).
 - [14] Yang Zhou and Peng Zhang, “Theory of field emission from dielectric coated surfaces,” *Physical Review Research* **2**, 043439 (2020).
 - [15] Christian Henkel, Robert Zierold, Adithya Kommini, Stefanie Haugg, Chris Thomason, Zlatan Aksamija, and Robert H Blick, “Resonant tunneling induced enhancement of electron field emission by ultra-thin coatings,” *Scientific Reports* **9**, 6840 (2019).
 - [16] Xi Tan, Paul Rumbach, Nathaniel Griggs, Kevin L Jensen, and David B Go, “Theoretical analysis of 1D resonant tunneling behavior in ion-enhanced cold field and thermo-field emission,” *Journal of Applied Physics* **120**, 213301 (2016).
 - [17] Yang Zhou, Ragib Ahsan, Hyun Uk Chae, Rehan Kapadia, and Peng Zhang, “Theoretical analysis of resonant tunneling enhanced field emission,” *Physical Review Applied* **20**, 014043 (2023).
 - [18] Michael V Davidovich, Igor S Nefedov, Olga E Glukhova, Michael M Slepchenkov, and J Miguel Rubi, “Field emission in vacuum resonant tunneling heterostructures with high current densities,” *Scientific Reports* **13**, 19365 (2023).
 - [19] Linjie Fan, Jinshun Bi, Kai Xi, Biyao Zhao, Xueqin Yang, and Yannan Xu, “Sub-10-nm air channel field emission device with ultra-low operating voltage,” *IEEE Electron Device Letters* **42**, 1390–1393 (2021).
 - [20] Wen-Teng Chang, Ming-Chih Cheng, Tsung-Ying Chuang, and Ming-Yen Tsai, “Field emission air-channel devices as a voltage adder,” *Nanomaterials* **10**, 2378 (2020).
 - [21] Minglei Tang, Chicheng Ma, Lining Liu, Xiaolong Tan, Yan Li, Young Jin Lee, Guodong Wang, Dae-Woo Jeon, Ji-Hyeon Park, Yiyun Zhang, *et al.*, “ β -Ga₂O₃ air-channel field-emission nanodiode with ultrahigh current density and low turn-on voltage,” *Nano Letters* **24**, 1769–1775 (2024).
 - [22] Keshab R Sapkota, François Leonard, A Alec Talin, Brendan P Gunning, Barbara A Kazanowska, Kevin S Jones, and George T Wang, “Ultralow voltage GaN vacuum nanodiodes in air,” *Nano Letters* **21**, 1928–1934 (2021).
 - [23] Wen-Teng Chang, Hsu-Jung Hsu, and Po-Heng Pao, “Vertical field emission air-channel diodes and transistors,” *Micromachines* **10**, 858 (2019).
 - [24] Meng Liu, Tie Li, and Yuelin Wang, “SiC emitters for nanoscale vacuum electronics: A systematic study of cathode–anode gap by focused ion beam etching,” *Journal of Vacuum Science & Technology B* **35**, 031801 (2017).
 - [25] Wei Cao, Huiming Bu, Maud Vinet, Min Cao, Shinichi Takagi, Sungwoo Hwang, Tahir Ghani, and Kaustav Banerjee, “The future transistors,” *Nature* **620**, 501–515 (2023).
 - [26] Dhiren K Pradhan, David C Moore, A Matt Francis, Jacob Kupernik, W Joshua Kennedy, Nicholas R Glavin, Roy H Olsson III, and Deep Jariwala, “Materials for high-temperature digital electronics,” *Nature Reviews Materials* **9**, 790–807 (2024).
 - [27] Hisato Yamaguchi, Katsuhisa Murakami, Goki Eda, Takeshi Fujita, Pengfei Guan, Weichao Wang, Cheng Gong, Julien Boisse, Steve Miller, Muge Acik, *et al.*, “Field emission from atomically thin edges of reduced graphene oxide,” *ACS Nano* **5**, 4945–4952 (2011).
 - [28] Kostya S Novoselov, Andre K Geim, Sergei V Morozov, De-eng Jiang, Yanshui Zhang, Sergey V Dubonos, Irina V Grigorieva, and Alexandr A Firsov, “Electric field effect in atomically thin carbon films,” *Science* **306**, 666–669 (2004).
 - [29] Jiaojiao Zhao, Lu Li, Peixuan Li, Liyan Dai, Jingwei Dong, Lanying Zhou, Yizhe Wang, Peihang Zhang, Kunshan Ji, Yangkun Zhang, *et al.*, “Realization of 2D metals at the ångström thickness limit,” *Nature* **639**, 354–359 (2025).
 - [30] Ivo Pletikosić, Marko Kralj, Petar Pervan, Radovan Brako, Johann Coraux, A T Ndiaye, C Busse, and Th Michely, “Dirac cones and minigaps for graphene on Ir (111),” *Physical Review Letters* **102**, 056808 (2009).
 - [31] A Varykhalov, M R Scholz, Timur K Kim, and O Rader, “Effect of noble-metal contacts on doping and band gap of graphene,” *Physical Review B* **82**, 121101 (2010).
 - [32] Joseph M Wofford, Elena Starodub, Andrew L Walter, Shu Nie, Aaron Bostwick, Norman C Bartelt, Konrad Thürmer, Eli Rotenberg, Kevin F McCarty, and Oscar D Dubon, “Extraordinary epitaxial alignment of graphene islands on Au (111),” *New Journal of Physics* **14**, 053008 (2012).
 - [33] Xi-Zhou Qin, Wie-Liang Wang, Ning-Sheng Xu, Zhi-Bing Li, and Richard G Forbes, “Analytical treatment of cold field electron emission from a nanowall emitter, including quantum confinement effects,” *Proceedings of the Royal Society A: Mathematical, Physical and Engineering Sciences* **467**, 1029–1051 (2011).
 - [34] Yee Sin Ang, Hui Ying Yang, and L K Ang, “Universal scaling laws in Schottky heterostructures based on two-dimensional materials,” *Physical Review Letters* **121**, 056802 (2018).
 - [35] Maxim Trushin, “Theory of thermionic emission from a two-dimensional conductor and its application to a graphene-semiconductor Schottky junction,” *Applied*

- Physics Letters **112**, 171109 (2018).
- [36] Bruno Lepetit, “A quantum mechanical model of electron field emission from two dimensional materials. Application to graphene,” *Journal of Applied Physics* **129**, 144302 (2021).
- [37] Wei Jie Chan, Chery Chua, Yee Sin Ang, and Lay Kee Ang, “Field emission in emerging two-dimensional and topological materials: A perspective,” *IEEE Transactions on Plasma Science* **51**, 1656–1670 (2022).
- [38] Yee Sin Ang, Liemao Cao, and Lay Kee Ang, “Physics of electron emission and injection in two-dimensional materials: theory and simulation,” *InfoMat* **3**, 502–535 (2021).
- [39] Jianmin Tao, Hong Tang, Abhirup Patra, Puskar Bhattarai, and John P Perdew, “Modeling the physisorption of graphene on metals,” *Physical Review B* **97**, 165403 (2018).
- [40] Yanpeng Liu, Li Yuan, Ming Yang, Yi Zheng, Linjun Li, Libo Gao, Nisachol Nerngchamnong, Chang Tai Nai, CS Suchand Sangeeth, Yuan Ping Feng, *et al.*, “Giant enhancement in vertical conductivity of stacked CVD graphene sheets by self-assembled molecular layers,” *Nature Communications* **5**, 5461 (2014).
- [41] Yu S Dedkov, M Fonin, U Rüdiger, and C Laubschat, “Rashba effect in the Graphene/Ni(111) system,” *Phys. Rev. Lett.* **100**, 107602 (2008).
- [42] G Giovannetti, P A Khomyakov, G Brocks, V M Karpan, J van den Brink, and P J Kelly, “Doping graphene with metal contacts,” *Phys. Rev. Lett.* **101**, 026803 (2008).
- [43] P A Khomyakov, G Giovannetti, P C Rusu, G Brocks, J van den Brink, and P J Kelly, “First-principles study of the interaction and charge transfer between graphene and metals,” *Phys. Rev. B* **79**, 195425 (2009).
- [44] Vahid Tayari, Andrew C McRae, Serap Yigen, Joshua O Island, James M Porter, and Alexandre R Champagne, “Tailoring 10 nm scale suspended graphene junctions and quantum dots,” *Nano Letters* **15**, 114–119 (2015).
- [45] Francois Leonard, *The Physics of Carbon Nanotube Devices, Chapter 6* (William Andrew, 2008).
- [46] Meng-Jey Youh, Chun-Lung Tseng, Meng-Han Jhuang, Sheng-Cheng Chiu, Li-Hu Huang, Jyun-An Gong, and Yuan-Yao Li, “Flat panel light source with lateral gate structure based on sic nanowire field emitters,” *Scientific Reports* **5**, 10976 (2015).
- [47] Xu Ji, Shi Yutong, Shi Yongjiao, Yang Wenxin, Wang Qilong, and Zhang Xiaobing, “Study on electrical properties and structure optimization of side-gate nanoscale vacuum channel transistor,” *Journal of Physics D: Applied Physics* **53**, 135301 (2020).
- [48] Zoltán Osváth, András Deák, Krisztián Kertész, Gy Molnár, Gábor Vértesy, Dániel Zámbo, Chanyong Hwang, and László P Biró, “The structure and properties of graphene on gold nanoparticles,” *Nanoscale* **7**, 5503–5509 (2015).
- [49] Edward McCann, David S L Abergel, and Vladimir I Fal’ko, “The low energy electronic band structure of bilayer graphene,” *The European Physical Journal Special Topics* **148**, 91–103 (2007).
- [50] Laxman Nagireddy, Samuel J Magorrian, Matthew D Watson, Yogal Prasad Ghimirey, Marc Walker, Cephise Cacho, Neil R Wilson, and Nicholas D M Hine, “Electronic structure of the interface between Au and WSe₂,” *2D Materials* **12**, 045017 (2025).
- [51] Shuhua Wang, Shibo Fang, Qiang Li, Yunliang Yue, Zongmeng Yang, Xiaotian Sun, Jing Lu, Chit Siang Lau, LK Ang, Lain-Jong Li, *et al.*, “Pressure-driven metallicity in ångström-thickness 2D bismuth and layer-selective ohmic contact to MoS₂,” *Nano Letters* **25**, 14550–14556 (2025).
- [52] Fengzhu Ren, Zhaoyang Han, Lingfeng Zhu, Zhihao Lei, Guozheng Shi, Zhixuan Li, Chun-Ho Lin, Long Hu, Hui Li, Xinwei Guan, *et al.*, “Metallene: Ångström-scale 2D metals,” *Advanced Materials*, e12683 (2025).
- [53] Julian Picker, Mahdi Ghorbani-Asl, Maximilian Schaal, Silvan Kretschmer, Felix Otto, Marco Gruenewald, Christof Neumann, Torsten Fritz, Arkady V Krasheninnikov, and Andrey Turchanin, “Atomic structure and electronic properties of janus SeMoS monolayers on Au (111),” *Nano Letters* **25**, 3330–3336 (2025).
- [54] Lili Xu, Shengli Zhang, and Yee Sin Ang, “Interface-dipole-driven type-II band offset engineering in perovskite heterostructures,” *Nano Letters* **25**, 18100–18107 (2025).
- [55] Chengfeng Pan, Jin Lv, Dazhong Sun, Zhennan Lin, Zifan Niu, Xiuyun Zhang, Xianghong Niu, and Yu-Ning Wu, “Layer-dependent asymmetric dipoles induced formation of atomically thin p-n junctions,” *Nano Letters* **25**, 17185–17193 (2025).

SUPPORTING INFORMATION

S1. Out-of-plane confinement for electrons in graphene

In general, electrons in a 2D conductor can be described by the Hamiltonian

$$\hat{H} = \hat{H}_{\parallel} + \hat{H}_{\perp}, \quad (\text{S1})$$

where \hat{H}_{\parallel} and \hat{H}_{\perp} describe in-plane and out-of-plane motion, respectively.

The in-plane Hamiltonian is typically derived from a tight-binding model that exploits lattice periodicity. For graphene, the low-energy tight-binding model on a honeycomb lattice with two interpenetrating sublattices yields the effective 2×2 Hamiltonian given by

$$\hat{H}_{\parallel} = \hbar v \begin{pmatrix} 0 & \hat{k}_x - i\hat{k}_y \\ \hat{k}_x + i\hat{k}_y & 0 \end{pmatrix}, \quad (\text{S2})$$

where $\hat{k}_{x,y}$ are the in-plane components of the electron wavevector, v is the tight-binding parameter (the effective Dirac velocity), and \hbar is the Planck constant. The spectrum of \hat{H}_{\parallel} is linear for both conduction and valence bands.

The out-of-plane term is less straightforward because there is no lattice periodicity along z . Instead, electrons experience very strong confinement leaving only the lowest quantized subband in a quantum well. A natural model for this situation is a delta-function confinement that supports a single bound state along z , see Fig. S1(a). The out-of-plane Hamiltonian then reads

$$\hat{H}_{\perp} = \frac{\hbar^2 \hat{k}_z^2}{2m_0} - u_0 \delta(z), \quad (\text{S3})$$

where u_0 is the confinement parameter (determined below), and m_0 is the free electron mass.

The eigen-states of \hat{H} can then be written as

$$\psi_0(x, y, z) = \frac{1}{L\sqrt{l_0}} e^{ik_x x + ik_y y - |z|/l_0} \begin{pmatrix} 1 \\ \pm e^{i\theta} \end{pmatrix}, \quad (\text{S4})$$

where $\tan \theta = k_y/k_x$, and the eigen-values are given by

$$E_{\pm} = \pm \hbar v k_{\parallel} - E_0, \quad (\text{S5})$$

where $k_{\parallel} = \sqrt{k_x^2 + k_y^2}$, and $E_0 = m_0 u_0^2 / (2\hbar^2)$ is the energy difference between the vacuum level and the charge neutrality point. The typical value of E_0 is about 4.6 eV, which corresponds to the work function of pristine (intrinsic) graphene. Equivalently, $E_0 = \hbar^2 / (2m_0 l_0^2)$, with a characteristic confinement length $l_0 = \hbar^2 / (m_0 u_0)$ of about an angstrom. If graphene is doped, the work function becomes $W = E_0 + \Delta E_F$, where ΔE_F is the Fermi level shift ($\Delta E_F < 0$ for n -type and $\Delta E_F > 0$ for p -type doping).

Delta-shaped confinement in an external field

Applying a uniform out-of-plane field \mathcal{E}_{ext} from $z = -\infty$ to $z = +\infty$ does not make much sense, as it renders the electron motion unbounded and eliminates bound states. Instead we introduce a potential drop ΔV at a distance $z = d$ from the origin point, see Fig. S1(b). The electric field is then taken to be constant, $\Delta V/d$, for $0 < z < d$, and to vanish outside this region. The out-of-plane wave function can be written as

$$\psi(z) = \begin{cases} A_1 e^{\kappa z}, & z < 0, \\ A_2 \text{Ai}(\zeta) + B_2 \text{Bi}(\zeta), & 0 < z < d, \\ A_3 e^{-\kappa z}, & z > d; \end{cases} \quad (\text{S6})$$

where $\kappa = \sqrt{-2m_0 E_{\kappa} / \hbar^2}$, $\text{Ai}(\zeta)$, $\text{Bi}(\zeta)$ are the Airy functions of ζ given by

$$\zeta = -\frac{E_{\kappa} d}{\Delta V z_0} + \frac{z}{z_0}, \quad (\text{S7})$$

$$z_0 = \left(\frac{\hbar^2 d}{2m_0 \Delta V} \right)^{\frac{1}{3}}, \quad (\text{S8})$$

and $E_{\kappa} = -E_0$ is the new bound-state energy to be found. The continuity conditions for $\psi(z)$ and $\psi'_z(z)$ result in the following set of four equations

$$\begin{cases} A_1 = A_2 \text{Ai}(\zeta_0) + B_2 \text{Bi}(\zeta_0), \\ A_1 \kappa - \frac{1}{z_0} [A_2 \text{Ai}'(\zeta_0) + B_2 \text{Bi}'(\zeta_0)] = \frac{2}{l_0} A_1, \\ A_2 \text{Ai}(\zeta_d) + B_2 \text{Bi}(\zeta_d) = A_3 e^{-\kappa d}, \\ \frac{1}{z_0} [A_2 \text{Ai}'(\zeta_d) + B_2 \text{Bi}'(\zeta_d)] = -A_3 \kappa e^{-\kappa d}, \end{cases} \quad (\text{S9})$$

where $\zeta_{0,d}$ are given by ζ taken at $z = 0, d$. The set of equations determines the coefficients $A_{1,2,3}$ and B_2 , as well as the binding energy E_0 . Excluding the coefficients A_1 and A_3 we obtain a set of two equations given by

$$A_2 \left[\kappa \text{Ai}(\zeta_0) - \frac{1}{z_0} \text{Ai}'(\zeta_0) - \frac{2}{l_0} \text{Ai}(\zeta_0) \right] + B_2 \left[\kappa \text{Bi}(\zeta_0) - \frac{1}{z_0} \text{Bi}'(\zeta_0) - \frac{2}{l_0} \text{Bi}(\zeta_0) \right] = 0, \quad (\text{S10})$$

$$A_2 \left[\kappa \text{Ai}(\zeta_d) + \frac{1}{z_0} \text{Ai}'(\zeta_d) \right] + B_2 \left[\kappa \text{Bi}(\zeta_d) + \frac{1}{z_0} \text{Bi}'(\zeta_d) \right] = 0. \quad (\text{S11})$$

The set of equations has a non-trivial solution when the determinant vanishes, hence, the eigen-value equation reads

$$\begin{aligned} & \left[\kappa \text{Ai}(\zeta_0) - \frac{1}{z_0} \text{Ai}'(\zeta_0) - \frac{2}{l_0} \text{Ai}(\zeta_0) \right] \left[\kappa \text{Bi}(\zeta_d) + \frac{1}{z_0} \text{Bi}'(\zeta_d) \right] \\ & - \left[\kappa \text{Bi}(\zeta_0) - \frac{1}{z_0} \text{Bi}'(\zeta_0) - \frac{2}{l_0} \text{Bi}(\zeta_0) \right] \\ & \times \left[\kappa \text{Ai}(\zeta_d) + \frac{1}{z_0} \text{Ai}'(\zeta_d) \right] = 0. \end{aligned} \quad (\text{S12})$$

The case of a negative potential drop at $z = -d$ shown in Fig. S1(c) can be considered in a similar way. Note that the potential gradient is still the same as in Fig. S1(b) and given by $\Delta V/d$. The wave function then reads

$$\psi(z) = \begin{cases} A_1 e^{\kappa z}, & z < -d, \\ A_2 \text{Ai}(\zeta) + B_2 \text{Bi}(\zeta), & -d < z < 0, \\ A_3 e^{-\kappa z}, & z > 0; \end{cases} \quad (\text{S13})$$

and the boundary conditions lead to the following set of equations

$$\begin{cases} A_1 e^{-\kappa d} = A_2 \text{Ai}(\zeta_{\bar{d}}) + B_2 \text{Bi}(\zeta_{\bar{d}}), \\ A_1 \kappa e^{-\kappa d} = \frac{1}{z_0} [A_2 \text{Ai}'(\zeta_{\bar{d}}) + B_2 \text{Bi}'(\zeta_{\bar{d}})], \\ A_2 \text{Ai}(\zeta_0) + B_2 \text{Bi}(\zeta_0) = A_3, \\ \frac{1}{z_0} [A_2 \text{Ai}'(\zeta_0) + B_2 \text{Bi}'(\zeta_0)] + A_3 \kappa = \frac{2}{l_0} A_3, \end{cases} \quad (\text{S14})$$

where $\zeta_{\bar{d}}$ is given by ζ taken at $z = -d$. The set can be simplified as follows

$$A_2 \left[\kappa \text{Ai}(\zeta_{\bar{d}}) - \frac{1}{z_0} \text{Ai}'(\zeta_{\bar{d}}) \right] + B_2 \left[\kappa \text{Bi}(\zeta_{\bar{d}}) - \frac{1}{z_0} \text{Bi}'(\zeta_{\bar{d}}) \right] = 0, \quad (\text{S15})$$

$$A_2 \left[\frac{2}{l_0} \text{Ai}(\zeta_0) - \frac{1}{z_0} \text{Ai}'(\zeta_0) - \kappa \text{Ai}(\zeta_0) \right] + B_2 \left[\frac{2}{l_0} \text{Bi}(\zeta_0) - \frac{1}{z_0} \text{Bi}'(\zeta_0) - \kappa \text{Bi}(\zeta_0) \right] = 0. \quad (\text{S16})$$

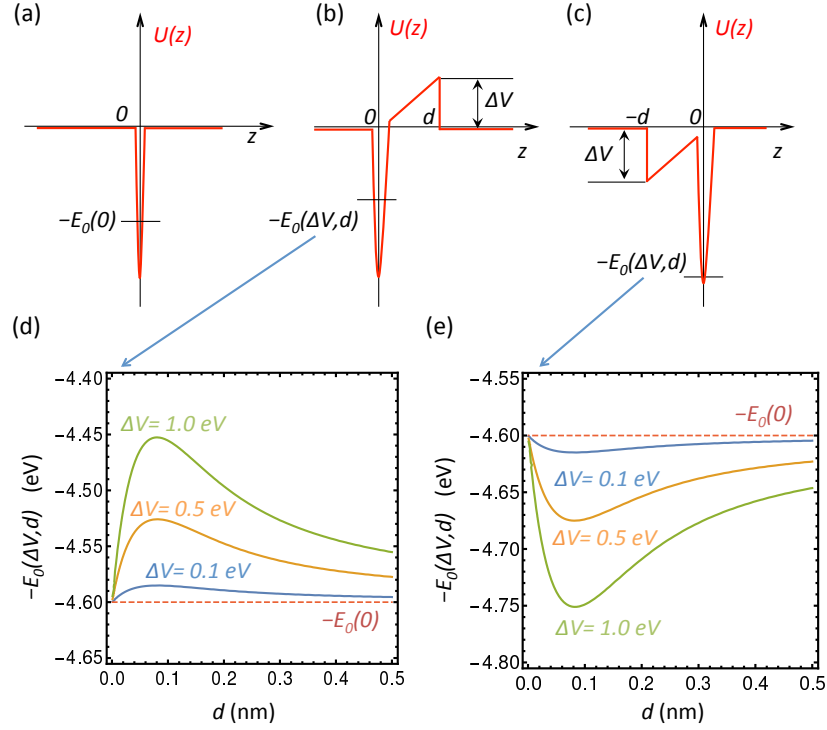


FIG. S1. Out-of-plane confinement of electrons in graphene modeled by a delta-function potential. (a) Electrons in an isolated delta-function potential have a single bound state at energy $-E_0$ corresponding to the difference between the vacuum level and the charge-neutrality (band-crossing) point in intrinsic (undoped) graphene. (b,c) An applied electrostatic potential shifts $-E_0$ up or down depending on its sign. The potential gradient $\Delta V/d$ may arise from a built-in field at the graphene-metal interface or from an external field. (d,e) Solutions of Eqs. (S12) and (S17) showing the shift of $-E_0$ for different ΔV and d . The shift is maximized at $d \sim l_0$ of about an angstrom, reaching a few tens of meV for a potential drop on the order of 0.1 eV.

The eigen-value equation reads

$$\begin{aligned} & \left[\kappa \text{Ai}(\zeta_{\bar{d}}) - \frac{1}{z_0} \text{Ai}'(\zeta_{\bar{d}}) \right] \left[\frac{2}{l_0} \text{Bi}(\zeta_0) - \frac{1}{z_0} \text{Bi}'(\zeta_0) - \kappa \text{Bi}(\zeta_0) \right] \\ & - \left[\kappa \text{Bi}(\zeta_{\bar{d}}) - \frac{1}{z_0} \text{Bi}'(\zeta_{\bar{d}}) \right] \\ & \times \left[\frac{2}{l_0} \text{Ai}(\zeta_0) - \frac{1}{z_0} \text{Ai}'(\zeta_0) - \kappa \text{Ai}(\zeta_0) \right] = 0. \end{aligned} \quad (\text{S17})$$

The solutions of Eqs. (S12,S17) are shown in Fig. S1(d,e), respectively. The potential drop ΔV in Fig. S1(d) can be interpreted as a built-in potential at a graphene-metal interface. For a graphene-metal spacing of a few angstroms, a built-in potential of 1 eV can raise the band-crossing point toward the vacuum level by about 100 meV. If the Fermi level is fixed, then graphene becomes *p*-doped. Figure S1(e) illustrates the effect of an external electric field, $\mathcal{E}_{\text{ext}} = \Delta V/d$, on the band-crossing point shift. Here, the field shifts the the band-crossing point downward, and graphene becomes *n*-doped. In this case, additional bound states may appear in the small triangular quantum well adjacent to the main delta-

function confinement, but they occur at a different energy scale and are not shown. In both cases, the energy shift vanishes at $d \gg l_0$.

Double-layer confinement in an external field

Let us consider the double-layer confinement, when the out-of-plane electron motion is limited by a pair of delta-functions, Fig. S2(a). The wave function can be written as

$$\psi(z) = \begin{cases} A_1 e^{\kappa z}, & z < -\frac{t}{2}, \\ A_2 e^{\kappa z} + B_2 e^{-\kappa z}, & -\frac{t}{2} < z < \frac{t}{2}, \\ A_3 e^{-\kappa z}, & z > \frac{t}{2}; \end{cases} \quad (\text{S18})$$

where t is the interlayer separation. Imposing the continuity conditions on $\psi(z)$ and $\psi'_z(z)$ at $z = \pm \frac{t}{2}$ we obtain

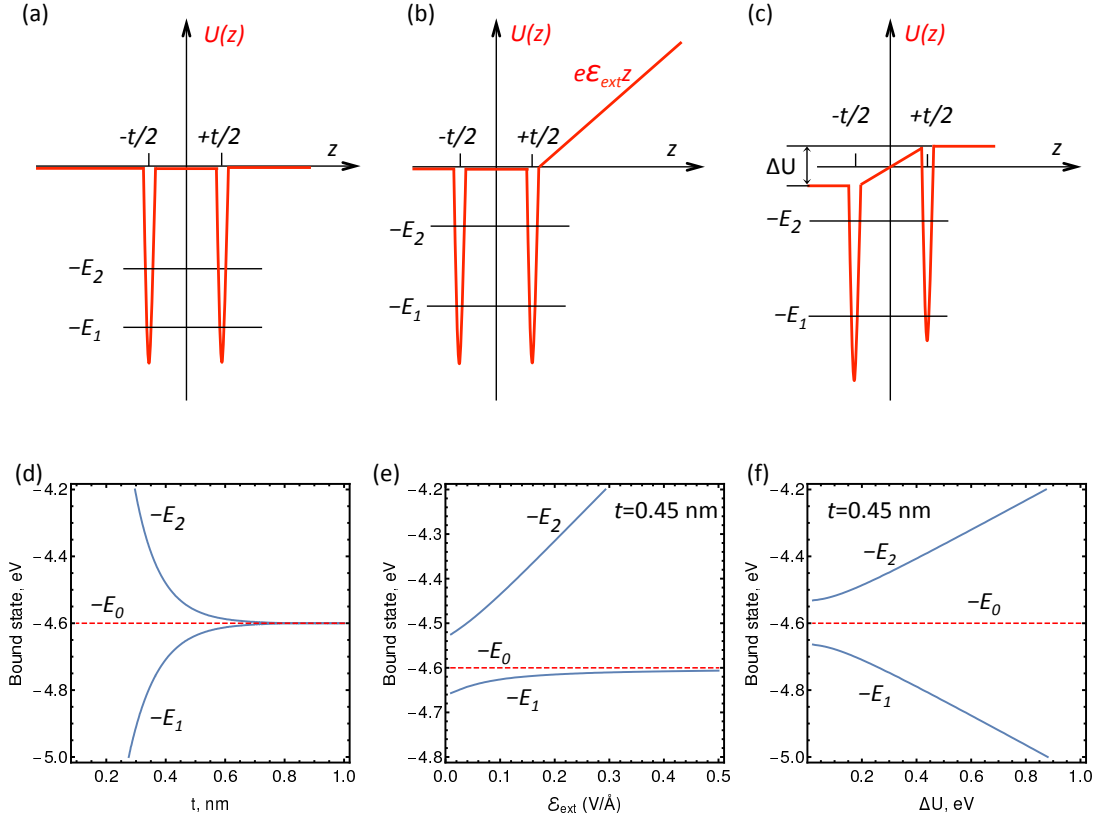


FIG. S2. Out-of-plane confinement of electrons in a double layer modeled by a pair of delta-function potentials. (a) An isolated double-delta potential supports two bound states at energies $-E_1$ and $-E_2$ corresponding to the even and odd parity, respectively. (b) An external field applied to one side of the double layer models electrostatic gating or the proximity effect of a metal. (c) Internal polarization of the double layer is included via a potential drop ΔU . (d) As the interlayer separation t decreases, the bound-state energy splitting $E_1 - E_2$ increases reaching a few hundred meV at t of a few angstroms, comparable to band splittings in bilayer graphene within a four-band model. Solution is given by Eq. (S20). (e) An applied field \mathcal{E}_{ext} drives the lower bound state E_1 toward the bound state of an isolated single-delta potential, while E_2 moves toward the continuum. Solution is given by Eq. (S25). (f) Interlayer polarization enhances the splitting $E_1 - E_2$. Solution is given by Eq. (S31).

the following set of four equations

$$\begin{cases} A_1 e^{-\kappa \frac{t}{2}} = A_2 e^{-\kappa \frac{t}{2}} + B_2 e^{\kappa \frac{t}{2}}, \\ A_1 \kappa e^{-\kappa \frac{t}{2}} - \kappa (A_2 e^{-\kappa \frac{t}{2}} - B_2 e^{\kappa \frac{t}{2}}) = \frac{2}{l_0} A_1 e^{-\kappa \frac{t}{2}}, \\ A_2 e^{\kappa \frac{t}{2}} + B_2 e^{-\kappa \frac{t}{2}} = A_3 e^{-\kappa \frac{t}{2}}, \\ \kappa (A_2 e^{\kappa \frac{t}{2}} - B_2 e^{-\kappa \frac{t}{2}}) + A_3 \kappa e^{-\kappa \frac{t}{2}} = \frac{2}{l_0} A_3 e^{-\kappa \frac{t}{2}}. \end{cases} \quad (\text{S19})$$

Excluding A_1 and A_3 we reduce the number of equations to two, and the eigen-value equation reads

$$\frac{1}{l_0^2 \kappa^2} - \left(\frac{1}{l_0 \kappa} - 1 \right)^2 e^{2\kappa t} = 0. \quad (\text{S20})$$

Eq. (S20) has two solutions $\kappa_{1,2}$ related to two energy eigen-values $-E_{1,2}$ as $\kappa_{1,2} = \sqrt{2m_0 E_{1,2}/\hbar^2}$. The state '1' is even, and the state '2' is odd. The eigen-values $-E_{1,2}$ are shown in Fig. S2(d) versus interlayer separation t . When the interlayer separation becomes of atomic scale,

$E_{1,2}$ degeneracy is lifted, doubling both the number of subbands and the number of resonance peaks. For bilayer graphene, this results in four bands rather than two in the multilayer limit.

When an external electric field is applied to one side of the double-layer junction, as shown in Fig. S2(b), the wave function reads

$$\psi(z) = \begin{cases} A_1 e^{\kappa z}, & z < -\frac{t}{2}, \\ A_2 e^{\kappa z} + B_2 e^{-\kappa z}, & -\frac{t}{2} < z < \frac{t}{2}, \\ A_3 \text{Ai}(\zeta), & z > \frac{t}{2}; \end{cases} \quad (\text{S21})$$

where

$$\zeta = -\frac{E_\kappa}{e\mathcal{E}_{\text{ext}}z_0} + \frac{z}{z_0}, \quad (\text{S22})$$

$$z_0 = \left(\frac{\hbar^2}{2m_0 e\mathcal{E}_{\text{ext}}} \right)^{\frac{1}{3}}, \quad (\text{S23})$$

and $E_\kappa = -E_{1,2}$ are the new bound-state energies to be found below. The continuity conditions imply the following equations

$$\begin{cases} A_1 e^{-\kappa \frac{t}{2}} = A_2 e^{-\kappa \frac{t}{2}} + B_2 e^{\kappa \frac{t}{2}}, \\ A_1 \kappa e^{-\kappa \frac{t}{2}} - \kappa (A_2 e^{-\kappa \frac{t}{2}} - B_2 e^{\kappa \frac{t}{2}}) = \frac{2}{l_0} A_1 e^{-\kappa \frac{t}{2}}, \\ A_2 e^{\kappa \frac{t}{2}} + B_2 e^{-\kappa \frac{t}{2}} = A_3 \text{Ai}(\zeta_{+\frac{t}{2}}), \\ \kappa (A_2 e^{\kappa \frac{t}{2}} - B_2 e^{-\kappa \frac{t}{2}}) + \frac{A_3}{z_0} \text{Ai}'(\zeta_{+\frac{t}{2}}) = \frac{2A_3}{l_0} \text{Ai}(\zeta_{+\frac{t}{2}}), \end{cases} \quad (\text{S24})$$

where $\zeta_{+\frac{t}{2}}$ is ζ taken at $z = \frac{t}{2}$. Note that $\text{Ai}(\zeta)$ vanishes at $z \rightarrow \infty$ so that no additional boundary condition is required to keep the wave function finite. Excluding A_1 and A_3 we reduce the number of equations to two, calculate the determinant obtaining the eigen-value equation given by

$$\begin{aligned} & \frac{1}{l_0 \kappa} \left(\frac{1}{l_0 \kappa} + \frac{1}{2} + \frac{1}{2z_0 \kappa} \frac{\text{Ai}'(\zeta_{+\frac{t}{2}})}{\text{Ai}(\zeta_{+\frac{t}{2}})} \right) \\ & - \left(\frac{1}{l_0 \kappa} - 1 \right) \left(\frac{1}{l_0 \kappa} - \frac{1}{2} + \frac{1}{2z_0 \kappa} \frac{\text{Ai}'(\zeta_{+\frac{t}{2}})}{\text{Ai}(\zeta_{+\frac{t}{2}})} \right) e^{2\kappa t} \\ & = 0. \end{aligned} \quad (\text{S25})$$

The eigen-values $-E_{1,2}$ are shown in Fig. S2(e) versus external field \mathcal{E}_{ext} . The applied field breaks mirror symmetry and increases the resonance splitting. Interestingly, the field drives the lower bound state E_1 toward the bound state of an isolated single-delta potential, E_0 .

Polarized double-layer can be modelled by means of a potential drop between the layers, ΔU , which can be related to the polarization field $P = \Delta U/(et)$, see Fig. S2(c). The wave function then reads

$$\psi(z) = \begin{cases} A_1 e^{\kappa+z}, & z < -\frac{t}{2}, \\ A_2 \text{Ai}(\zeta) + B_2 \text{Bi}(\zeta), & -\frac{t}{2} < z < \frac{t}{2}, \\ A_3 e^{-\kappa-z}, & z > \frac{t}{2}; \end{cases} \quad (\text{S26})$$

where $\kappa_\pm = \sqrt{-2m_0 (E_\kappa \pm \frac{\Delta U}{2})/\hbar^2}$, and ζ is given by

$$\zeta = -\frac{E_\kappa t}{\Delta U z_0} + \frac{z}{z_0}, \quad (\text{S27})$$

$$z_0 = \left(\frac{\hbar^2 t}{2m_0 \Delta U} \right)^{\frac{1}{3}}. \quad (\text{S28})$$

Imposing the boundary conditions we arrive at the following set of equations

$$\begin{cases} A_1 e^{-\kappa+\frac{t}{2}} = A_2 \text{Ai}(\zeta_{-\frac{t}{2}}) + B_2 \text{Bi}(\zeta_{-\frac{t}{2}}), \\ A_1 \kappa + e^{-\kappa \frac{t}{2}} - \frac{1}{z_0} [A_2 \text{Ai}'(\zeta_{-\frac{t}{2}}) + B_2 \text{Bi}'(\zeta_{-\frac{t}{2}})] \\ = \frac{2}{l_0} A_1 e^{-\kappa+\frac{t}{2}}, \\ A_2 \text{Ai}(\zeta_{+\frac{t}{2}}) + B_2 \text{Bi}(\zeta_{+\frac{t}{2}}) = A_3 e^{-\kappa-\frac{t}{2}}, \\ \frac{1}{z_0} [A_2 \text{Ai}'(\zeta_{+\frac{t}{2}}) + B_2 \text{Bi}'(\zeta_{+\frac{t}{2}})] + A_3 \kappa_- e^{-\kappa-\frac{t}{2}} \\ = \frac{2}{l_0} A_3 e^{-\kappa-\frac{t}{2}}. \end{cases} \quad (\text{S29})$$

Excluding A_1 and A_3 we have a set of two equations given by

$$\begin{aligned} & A_2 \left[\frac{2}{l_0} \text{Ai}(\zeta_{-\frac{t}{2}}) - \kappa_+ \text{Ai}(\zeta_{-\frac{t}{2}}) + \frac{1}{z_0} \text{Ai}'(\zeta_{-\frac{t}{2}}) \right] \\ & + B_2 \left[\frac{2}{l_0} \text{Bi}(\zeta_{-\frac{t}{2}}) - \kappa_+ \text{Bi}(\zeta_{-\frac{t}{2}}) + \frac{1}{z_0} \text{Bi}'(\zeta_{-\frac{t}{2}}) \right] = 0 \\ & A_2 \left[\frac{2}{l_0} \text{Ai}(\zeta_{+\frac{t}{2}}) - \kappa_- \text{Ai}(\zeta_{+\frac{t}{2}}) - \frac{1}{z_0} \text{Ai}'(\zeta_{+\frac{t}{2}}) \right] \\ & + B_2 \left[\frac{2}{l_0} \text{Bi}(\zeta_{+\frac{t}{2}}) - \kappa_- \text{Bi}(\zeta_{+\frac{t}{2}}) - \frac{1}{z_0} \text{Bi}'(\zeta_{+\frac{t}{2}}) \right] = 0. \end{aligned} \quad (\text{S30})$$

The eigen-value equation then reads

$$\begin{aligned} & \left[\frac{2}{l_0} \text{Ai}(\zeta_{-\frac{t}{2}}) - \kappa_+ \text{Ai}(\zeta_{-\frac{t}{2}}) + \frac{1}{z_0} \text{Ai}'(\zeta_{-\frac{t}{2}}) \right] \\ & \times \left[\frac{2}{l_0} \text{Bi}(\zeta_{+\frac{t}{2}}) - \kappa_- \text{Bi}(\zeta_{+\frac{t}{2}}) - \frac{1}{z_0} \text{Bi}'(\zeta_{+\frac{t}{2}}) \right] \\ & - \left[\frac{2}{l_0} \text{Bi}(\zeta_{-\frac{t}{2}}) - \kappa_+ \text{Bi}(\zeta_{-\frac{t}{2}}) + \frac{1}{z_0} \text{Bi}'(\zeta_{-\frac{t}{2}}) \right] \\ & \times \left[\frac{2}{l_0} \text{Ai}(\zeta_{+\frac{t}{2}}) - \kappa_- \text{Ai}(\zeta_{+\frac{t}{2}}) - \frac{1}{z_0} \text{Ai}'(\zeta_{+\frac{t}{2}}) \right] \\ & = 0. \end{aligned} \quad (\text{S31})$$

Eq. (S31) can be solved with respect E_κ to find two solutions $-E_{1,2}$ shown in Fig. S2(f). The energy splitting $E_1 - E_2$ increases with increasing polarization, as expected.

S2. Field emission from a bare metal

Field electron emission from a bare metal is usually calculated within the Wentzel-Kramers-Brillouin (WKB)

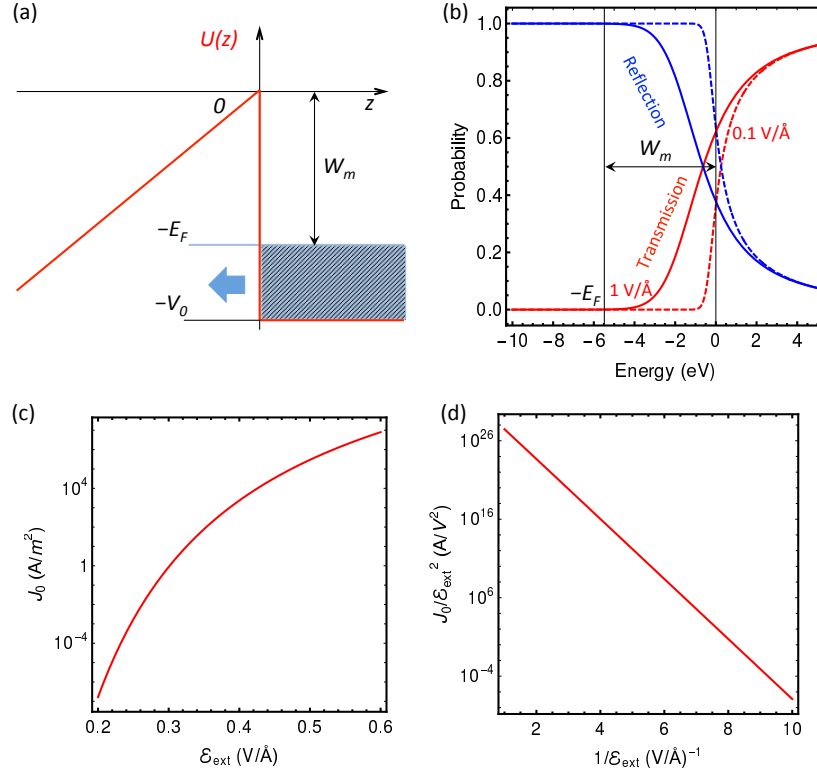


FIG. S3. Electron field emission from a metal without graphene. (a) Potential profile $U(z)$ in an external field \mathcal{E}_{ext} . Here $W_m = E_F$ is the metal work function, $E_F > 0$ is the Fermi energy (measured from the vacuum level), $V_0 > 0$ is the conduction-band depth, and the energy interval between $-V_0$ and $-E_F$ is occupied by electrons. (b) Transmission and reflection probabilities versus energy referenced to from the vacuum level. Solid curves: $\mathcal{E}_{\text{ext}} = 1 \text{ V/\AA}$; dashed curves: $\mathcal{E}_{\text{ext}} = 0.1 \text{ V/\AA}$. (c) Field emission current density as a function of \mathcal{E}_{ext} . Electron-electron interactions (e.g., image-charge effects) are neglected, which overestimates the field required to obtain a measurable current. (d) Fowler-Nordheim representation showing a linear relation between $\ln(J_0/\mathcal{E}_{\text{ext}}^2)$ and $1/\mathcal{E}_{\text{ext}}$.

approximation. However, we use an exact solution here, because resonant tunneling occurring in the presence of graphene is not tractable semiclassically. The potential profile is shown in Fig. S3(a). The wave function can be written in terms of the Airy functions Ai and Bi as

$$\psi(z) = \begin{cases} A_1 [\text{Ai}(\zeta) + i\text{Bi}(\zeta)], & z < 0, \\ A_3 e^{-ikz} + B_3 e^{ikz}, & z > 0; \end{cases} \quad (\text{S32})$$

where ζ is given by

$$\zeta = -\frac{E_k}{e\mathcal{E}_{\text{ext}}z_0} + \frac{z}{z_0}, \quad (\text{S33})$$

$$z_0 = \left(\frac{\hbar^2}{2m_0 e \mathcal{E}_{\text{ext}}} \right)^{\frac{1}{3}}. \quad (\text{S34})$$

The total electron energy reads

$$E_{\text{tot}} = E_k + \frac{\hbar^2 k_{\parallel}^2}{2m}, \quad (\text{S35})$$

where $\hbar k_{\parallel}$ is the in-plane momentum, and

$$E_k = -V_0 + \frac{\hbar^2 k^2}{2m}, \quad (\text{S36})$$

where $\hbar k$ is the out-of-plane momentum. The amplitudes A_1 and A_3 can be found by matching the wave function and its derivative at $z = 0$ as

$$A_1 [\text{Ai}(\zeta_0) + i\text{Bi}(\zeta_0)] = A_3 + B_3 \quad (\text{S37})$$

$$\frac{A_1}{z_0} [\text{Ai}'(\zeta_0) + i\text{Bi}'(\zeta_0)] = -ikA_3 + ikB_3, \quad (\text{S38})$$

where ζ_0 is ζ taken at $z = 0$, and $\text{Ai}'(\zeta)$, $\text{Bi}'(\zeta)$ are the derivatives of the Airy functions. The incident and reflected probability current densities respectively read

$$j_i = \frac{\hbar k}{m} |B_3|^2, \quad j_r = \frac{\hbar k}{m} |A_3|^2, \quad (\text{S39})$$

whereas the transmitted probability current density is

given by

$$j_t = \frac{\hbar}{mz_0} |A_1|^2 [\text{Ai}(\zeta)\text{Bi}'(\zeta) - \text{Ai}'(\zeta)\text{Bi}(\zeta)] \quad (\text{S40})$$

$$= \frac{\hbar}{\pi m z_0} |A_1|^2. \quad (\text{S41})$$

The transmission and reflection probabilities can be written as

$$T = \frac{j_t}{j_i}, \quad R = \frac{j_r}{j_i}. \quad (\text{S42})$$

By convention, we take $k < 0$ for the incident current propagating toward $z \rightarrow -\infty$, and we set $B_3 = 1$ for normalization. The probabilities are shown in Fig. S3(b) for two different \mathcal{E}_{ext} .

The total electrical current density is calculated by integrating over occupied states in the metal weighted by the probability current density as

$$J_0 = 2e \int \frac{dk}{2\pi} \int \frac{d^2 k_{\parallel}}{(2\pi)^2} v_k T(k) \quad (\text{S43})$$

$$= 2e \int \frac{dk}{2\pi} \int \frac{d^2 k_{\parallel}}{(2\pi)^2} j_t(k). \quad (\text{S44})$$

where $v_k = \hbar k/m$. The subscript ‘‘0’’ in J_0 denotes the absence of graphene. The integration limits can be found from the following conditions

$$E_{\text{tot}} \leq -E_F \quad (\text{S45})$$

$$k_{\parallel} \leq \sqrt{\frac{2m}{\hbar^2} (-E_k - E_F)}, \quad (\text{S46})$$

and

$$-E_k - E_F \geq 0 \quad (\text{S47})$$

$$k \leq \sqrt{\frac{2m}{\hbar^2} (V_0 - E_F)}, \quad (\text{S48})$$

see Fig. S3(a) for V_0 and E_F .

Switching to the cylindrical coordinates and changing the integration variable we have

$$\begin{aligned} J_0 &= \frac{e}{(2\pi)^2} \int_{-V_0}^{-E_F} dE_k \frac{2m j_t \left(\sqrt{\frac{2m}{\hbar^2} (V_0 + E_k)} \right)}{\sqrt{\frac{2m}{\hbar^2} (V_0 + E_k)}} \\ &\quad \times \int_0^{\sqrt{\frac{2m}{\hbar^2} (-E_F - E_k)}} dk_{\parallel} k_{\parallel} \quad (\text{S49}) \\ &= \frac{e}{8\pi^2} \left(\frac{2m}{\hbar^2} \right)^{\frac{3}{2}} \int_{-V_0}^{-E_F} dE_k \frac{-E_F - E_k}{\sqrt{V_0 + E_k}} \\ &\quad \times j_t \left(\sqrt{\frac{2m}{\hbar^2} (V_0 + E_k)} \right). \quad (\text{S50}) \end{aligned}$$

The field emission current density described by equation (S50) follows the well known dependence on external field, as shown in Fig. S3 (c,d). We use J_0 given by equation (S50) to normalize the field emission current in the presence of graphene.

S3. Finite-size device simulations

In the field emission regime, transmission is typically modeled through a triangular barrier, assuming the anode is effectively at infinity. In this limit, the transmission probability is governed by the barrier shape rather than the cathode-anode separation. However, when the device is small or the field is weak, the separation becomes critical, distinguishing field emission from direct tunneling. Here, we consider the length explicitly including L into the solution given by

$$\psi(z) = \begin{cases} A_0 e^{-ipz} + B_0 e^{ipz}, & z < -L; \\ A_1 \text{Ai}(\zeta_1) + B_1 \text{Bi}(\zeta_1), & -L < z < 0, \\ A_2 \text{Ai}(\zeta_2) + B_2 \text{Bi}(\zeta_2), & 0 < z < d, \\ A_3 e^{-ikz} + B_3 e^{ikz}, & z > d; \end{cases} \quad (\text{S51})$$

$$\zeta_1 = -\frac{E_k}{e\mathcal{E}_{\text{ext}}z_1} + \frac{z}{z_1}, \quad z_1 = \left(\frac{\hbar^2}{2me\mathcal{E}_{\text{ext}}} \right)^{\frac{1}{3}}, \quad (\text{S52})$$

$$\zeta_2 = -\frac{E_k d}{\Delta V z_2} + \frac{z}{z_2}, \quad z_2 = \left(\frac{\hbar^2 d}{2m\Delta V} \right)^{\frac{1}{3}}, \quad (\text{S53})$$

$$k = \sqrt{\frac{2m}{\hbar^2} (V_0 + E_k)}, \quad (\text{S54})$$

$$p = \sqrt{\frac{2m}{\hbar^2} (V_0 + \Delta V + e\mathcal{E}_{\text{ext}}L + E_k)}. \quad (\text{S55})$$

By convention, we take $A_0 = 0$ and set $B_3 = 1$ for normalization. The remaining coefficients are found by matching the wave function and its derivative at $z = -L$, $z = 0$, and $z = d$ as

$$B_0 e^{-ipL} = A_1 \text{Ai}(\zeta_{1L}) + B_1 \text{Bi}(\zeta_{1L}), \quad (\text{S56})$$

$$ipB_0 e^{-ipL} = \frac{1}{z_1} [A_1 \text{Ai}'(\zeta_{1L}) + B_1 \text{Bi}'(\zeta_{1L})], \quad (\text{S57})$$

$$A_1 \text{Ai}(\zeta_{10}) + B_1 \text{Bi}(\zeta_{10}) = A_2 \text{Ai}(\zeta_{20}) + B_2 \text{Bi}(\zeta_{20}), \quad (\text{S58})$$

$$\frac{1}{z_1} [A_1 \text{Ai}'(\zeta_{10}) + B_1 \text{Bi}'(\zeta_{10})]$$

$$- \frac{1}{z_2} [A_2 \text{Ai}'(\zeta_{20}) + B_2 \text{Bi}'(\zeta_{20})]$$

$$= \frac{2}{l_0} [A_2 \text{Ai}(\zeta_{20}) + B_2 \text{Bi}(\zeta_{20})], \quad (\text{S59})$$

$$A_2 \text{Ai}(\zeta_{2d}) + B_2 \text{Bi}(\zeta_{2d}) = A_3 e^{-ikd} + B_3 e^{ikd}, \quad (\text{S60})$$

$$\frac{1}{z_2} [A_2 \text{Ai}'(\zeta_{2d}) + B_2 \text{Bi}'(\zeta_{2d})]$$

$$= -ikA_3 e^{-ikd} + ikB_3 e^{ikd}, \quad (\text{S61})$$

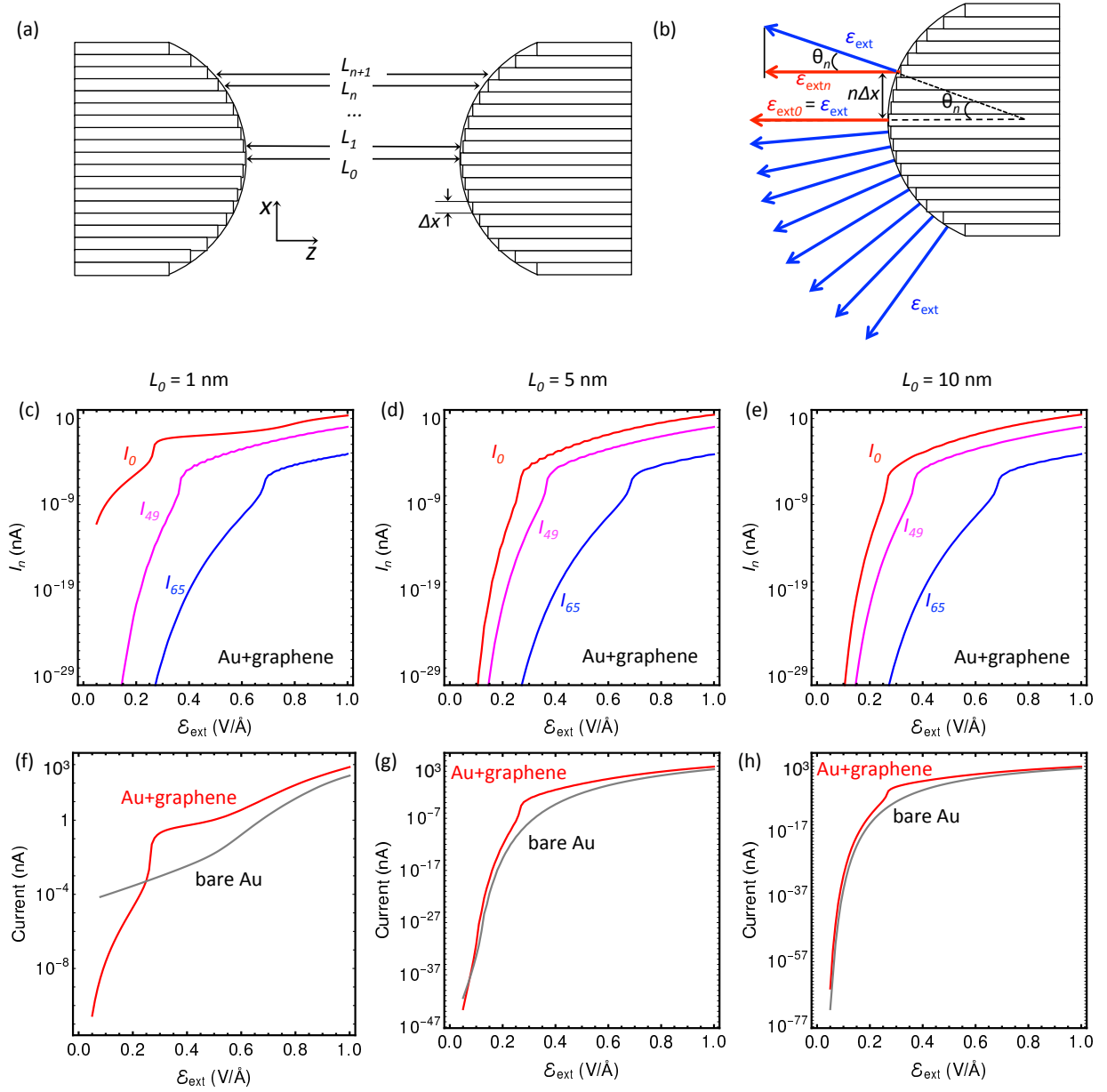


FIG. S4. Electrode surface curvature. (a) The electrodes are modeled as two nanorods with identical semicircular tips of radius $r_0 = 10$ nm and height of $\Delta y = 10$ nm. Each tip is partitioned into elementary emitters of area $\Delta x \Delta y$, separated by different path lengths L_n , see Eq. (S71) with $\Delta x = 1.42 \text{ \AA}$, and n is the integer $0, \dots, 70$. (b) The true electric field \mathcal{E}_{ext} (blue arrows) is everywhere normal to the metallic surface. For the partitioned surface, the effective field driving emission from the n -th emitter is the component along its local normal, $\mathcal{E}_{\text{ext}} \cos \theta_n$. (c,d,e) Emission current I_n for three representative elementary emitters and three electrode separations, see Eq. (S74). The central channel I_0 always dominates, indicating strongest emission from the apex. Oscillations in I_n arise from backscattering between the electrodes. (f,g,h) Total current obtained by summing all elementary contributions. Gray curves show the corresponding current for bare gold electrodes. The transition between direct tunneling and field emission is evident in (f) near $\sim 0.5 \text{ V/\AA}$ and in (g) near $\sim 0.1 \text{ V/\AA}$ as the intersection of gray and red curves. For $L_0 > 10$ nm, direct tunneling is negligible, so red and gray curves coincide in both low- and high-field limits, while a clear difference persists at the resonance field.

where $\zeta_{1L} = \zeta_1(z = L)$, $\zeta_{10} = \zeta_1(z = 0)$, $\zeta_{1d} = \zeta_1(z = d)$, $\zeta_{20} = \zeta_2(z = 0)$, $\zeta_{2d} = \zeta_2(z = d)$. Solving Eqs. (S56–S61) yields $A_{1,2,3}$ and $B_{0,2}$. The incident, reflected, and transmitted probability current densities are, respec-

tively, given by

$$j_i = \frac{\hbar k}{m} |B_3|^2, \quad j_r = \frac{\hbar k}{m} |A_3|^2, \quad j_t = \frac{\hbar p}{m} |B_0|^2. \quad (\text{S62})$$

If graphene is removed, then Eqs. (S56–S61) are re-

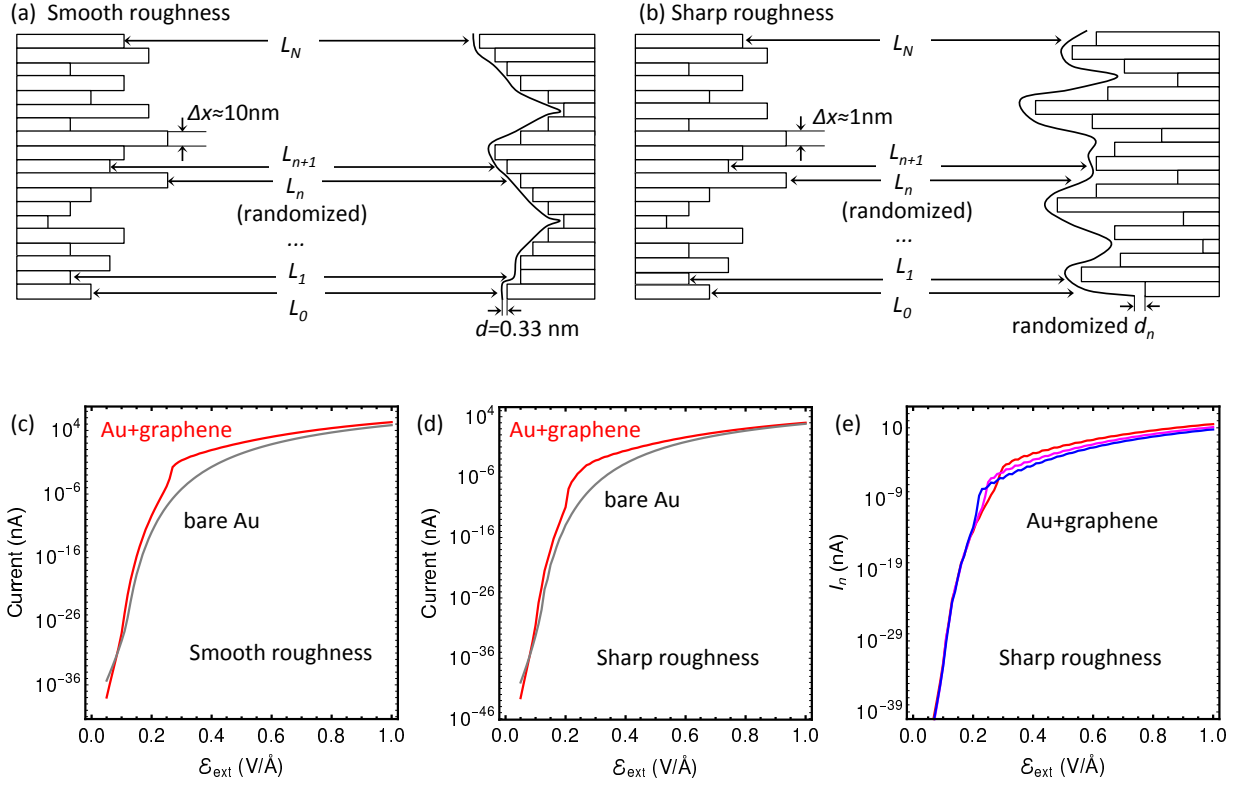


FIG. S5. Electrode surface roughness. (a) Smooth roughness, where the graphene layer conforms to the underlying metal surface profile and the graphene-metal separation remains approximately uniform. (b) Sharp roughness, where the graphene-metal separation is randomized. (c) Total emission current for smooth roughness, showing the same resonance feature as in the perfectly flat case. Gray curve corresponds to bare gold electrodes. Configuration: 100 channels, $\Delta x \Delta y = 100 \text{ nm}^2$ with L randomized in the interval 4.5–5.5 nm. (d) For sharp roughness, the resonance is broadened but remains visible. Configuration: 100 channels, $\Delta x \Delta y = 1 \text{ nm}^2$; L and d are independently randomized over 4.9–5.1 nm and 0.23–0.43 nm, respectively. (e) Emission currents I_n for three representative channels contributing to (d). Random resonance shifts in each channel flatten the overall resonance feature in (d).

duced to the following set

$$\zeta_1 = -\frac{E_k}{e\mathcal{E}_{\text{ext}}z_1} + \frac{z}{z_1}, \quad z_1 = \left(\frac{\hbar^2}{2me\mathcal{E}_{\text{ext}}}\right)^{\frac{1}{3}}, \quad (\text{S63})$$

$$\zeta_2 = -\frac{E_k d}{\Delta V z_2} + \frac{z}{z_2}, \quad z_2 = \left(\frac{\hbar^2 d}{2m\Delta V}\right)^{\frac{1}{3}}, \quad (\text{S64})$$

$$k = \sqrt{\frac{2m}{\hbar^2}(V_0 + E_k)}, \quad (\text{S65})$$

$$p = \sqrt{\frac{2m}{\hbar^2}(V_0 + \Delta V + e\mathcal{E}_{\text{ext}}L + E_k)}. \quad (\text{S66})$$

By convention, we take $A_0 = 0$ and set $B_3 = 1$ for normalization. The remaining coefficients are found by matching the wave function and its derivative at $z = -L$,

$z = 0$, and $z = d$ as

$$B_0 e^{-ipL} = A_1 \text{Ai}(\zeta_{1L}) + B_1 \text{Bi}(\zeta_{1L}), \quad (\text{S67})$$

$$ipB_0 e^{-ipL} = \frac{1}{z_1} [A_1 \text{Ai}'(\zeta_{1L}) + B_1 \text{Bi}'(\zeta_{1L})], \quad (\text{S68})$$

$$A_1 \text{Ai}(\zeta_0) + B_1 \text{Bi}(\zeta_0) = A_3 + B_3 \quad (\text{S69})$$

$$\frac{1}{z_0} [A_1 \text{Ai}'(\zeta_0) + B_1 \text{Bi}'(\zeta_0)] = -ikA_3 + ikB_3 \quad (\text{S70})$$

where ζ_0 is $\zeta(z = 0)$ determined by Eq. (S33). The incident, reflected, and transmitted probability current densities are defined in the same way as before. The finite-size solution allows us to model curved and uneven anode and cathode surfaces.

Let us start from smoothly curved electrodes, Fig. S4. By partitioning each surface into small, finite elementary emitters, we obtain a set of channels, each with a well-defined length L_n . If the radius of curvature (r_0) is constant and identical for both electrodes, then L_n is

given by

$$L_n = L_0 + 2r_0 - 2\sqrt{r_0^2 - (n\Delta x)^2}, \quad (\text{S71})$$

where L_0 is the length of the central (shortest) channel, and Δx is the channel width. The typical curvature of the gold nanorods considered here is $r_0 = 10$ nm. The natural width of an elementary emitter is set by graphene's lattice scale, we take $\Delta x = 1.42\text{\AA}$.

In addition to the length change, we have to model the field texture which is not collinear in the case of curved surface. The z-component of the electric field which drives the current between the electrodes is different for each elementary emitter and can be written as

$$\mathcal{E}_{\text{ext}n} = \mathcal{E}_{\text{ext}} \cos \theta_n \quad (\text{S72})$$

$$= \mathcal{E}_{\text{ext}} \sqrt{1 - \left(\frac{n\Delta x}{r_0}\right)^2}. \quad (\text{S73})$$

Using the results of the previous section, the emission current for the n -th channel can be written as

$$I_n = \frac{e\Delta x\Delta y}{8\pi^2} \left(\frac{2m}{\hbar^2}\right)^{\frac{3}{2}} \int_{-V_0}^{-E_F} dE_k \frac{-E_F - E_k}{\sqrt{V_0 + E_k}} \times j_t \left(\sqrt{\frac{2m}{\hbar^2} (V_0 + E_k)}, L_n, \mathcal{E}_{\text{ext}n} \right), \quad (\text{S74})$$

where $\Delta x\Delta y$ is the elementary cross section of a channel. The curvature of the field lines is not included in this approximation. Note that V_0 is defined differently depending on whether a graphene layer is present. The total current is then the sum over all channels, $I = \sum_n I_n$. The channel at the apex of a electrode (i.e. I_n with $n = 0$) dominates in field-emission because (i) the driving electric field is maximized ($\mathcal{E}_{\text{ext}0} = \mathcal{E}_{\text{ext}}$) and (ii) the channel length is minimized.

Finally, we address rough emitting surfaces. Two scenarios are relevant (Fig. S5): (1) smooth roughness, where the graphene conforms to the underlying metal topography and the graphene-metal separation d remains essentially constant; and (2) sharp roughness, where graphene can sag over local troughs, randomizing d within a finite range. Unlike the curved-tip case, in the planar geometry the driving electric field is the same for all elementary emitters. Hence, the emission current for the n -th channel reads

$$I_n = \frac{e\Delta x\Delta y}{8\pi^2} \left(\frac{2m}{\hbar^2}\right)^{\frac{3}{2}} \int_{-V_0}^{-E_F} dE_k \frac{-E_F - E_k}{\sqrt{V_0 + E_k}} \times j_t \left(\sqrt{\frac{2m}{\hbar^2} (V_0 + E_k)}, L_n, d_n \right), \quad (\text{S75})$$

where L_n and d_n are randomized within the respective intervals $L_{\text{max}} < L_n < L_{\text{min}}$, $d_{\text{max}} < d_n < d_{\text{min}}$.